SANDIA REPORT
SAND2021-13572
Printed October 2021

Sandia National Laboratories

Measuring Saturn's Electron Beam Energy Spectrum using Webb's Wedges

Ben A. Ulmen, Tim J. Webb, Andrew L. McCourt, Sean K. Coffey

Prepared by
Sandia National Laboratories
Albuquerque, New Mexico
87185 and Livermore,
California 94550

Issued by Sandia National Laboratories, operated for the United States Department of Energy by National Technology & Engineering Solutions of Sandia, LLC.

NOTICE: This report was prepared as an account of work sponsored by an agency of the United States Government. Neither the United States Government, nor any agency thereof, nor any of their employees, nor any of their contractors, subcontractors, or their employees, make any warranty, express or implied, or assume any legal liability or responsibility for the accuracy, completeness, or usefulness of any information, apparatus, product, or process disclosed, or represent that its use would not infringe privately owned rights. Reference herein to any specific commercial product, process, or service by trade name, trademark, manufacturer, or otherwise, does not necessarily constitute or imply its endorsement, recommendation, or favoring by the United States Government, any agency thereof, or any of their contractors or subcontractors. The views and opinions expressed herein do not necessarily state or reflect those of the United States Government, any agency thereof, or any of their contractors.

Printed in the United States of America. This report has been reproduced directly from the best available copy.

Available to DOE and DOE contractors from
U.S. Department of Energy
Office of Scientific and Technical Information
P.O. Box 62
Oak Ridge, TN 37831

Telephone: (865) 576-8401
Facsimile: (865) 576-5728
E-Mail: reports@osti.gov
Online ordering: http://www.osti.gov/scitech

Available to the public from
U.S. Department of Commerce
National Technical Information Service
5301 Shawnee Rd
Alexandria, VA 22312

Telephone: (800) 553-6847
Facsimile: (703) 605-6900
E-Mail: orders@ntis.gov
Online order: https://classic.ntis.gov/help/order-methods/

ABSTRACT

It is very difficult to measure the voltage of the load on the Saturn accelerator. Time-resolved measurements such as vacuum voltmeters and V-dot monitors are impractical at best and completely change the pulsed power behavior at the load at worst. We would like to know the load voltage of the machine so that we could correctly model the radiation transport and tune our x-ray unfold methodology and circuit simulations of the accelerator. Step wedges have been used for decades as a tool to measure the end-point energies of high energy particle beams. Typically, the technique is used for multi-megavolt accelerators, but we have adapted it to Saturn's modest <2 MV end-point energy and modified the standard bremsstrahlung x-ray source to extract the electron beam without changing the physics of the load region. We found clear evidence of high energy electrons >2 MV. We also attempted to unfold an electron energy spectrum using a machine learning algorithm and while these results come with large uncertainties, they qualitatively agree with PIC simulation results.

ACKNOWLEDGEMENTS

The authors would like thank Jim Moore for the use of his laboratory and pulser hardware to calibrate our B-dot current monitors.

We would like to thank the staff and crew of org. 1342 for their support during our Saturn experiment.

Thanks to Chris Grabowski for his effort to calibrate the V2 and B3 radiochromic films at the Gamma Irradiation Facility in TA-V.

Warren Davis was extremely helpful in his advice on how to setup and tune the neural network algorithm. Machine learning is still very much an art and Warren's tips helped us overcome our confusion about why the neural network predictor was getting stuck on training set data.

CONTENTS

LIST OF FIGURES

LIST OF TABLES

This page left blank

EXECUTIVE SUMMARY

The goal of this work was to test a new method of measuring the end-point energy of the electron beam of the Saturn 3-ring bremsstrahlung (brems) diode. In our effort to better understand the spectral output of this x-ray source, we wanted to measure the end-point energy of electron beam directly since this is effectively the source term in an electron-photon simulation of the radiation environment. This diode has no space for electrical diagnostics so we thought we could extract the electron beam through a thin anode foil so that it would scatter but not lose too much energy and then deposit into an aluminum wedge with radiochromic films sandwiched inside. This wedge technique had been used successfully on the RITS-6 accelerator. However, that machine has a much larger end-point energy and so the penetration depth of the electron beam is large and interpreting the films is straightforward. For Saturn's much small end-point energy, the penetration depth is small and therefore the wedge would have to be very shallow. We were uncertain whether the beam scattering through the pinhole in the beamstop would expand uniformly to fill the wedge or if it would pinch and be impossible to interpret. We also had concerns about our ability to measure the beam current.

We performed a week-long experiment at Saturn in 2019 to test this concept. We designed the hardware to keep the conditions in the diode the same. That means the converter was still tantalum, but only $1/10^{th}$ the thickness of the standard converter. This was the first attempt to run "decoupled", meaning that the polyethylene beamstop was not tied to the upper anode through the diode feed. This was done purely for practical considerations because we used the flat-top dome instead of the bremsstrahlung dome, but this is now standard practice for the diode setup. Three shots were taken with the last two being the primary focus of the analysis. For the first shot, we found the beams were misaligned with the pinholes, they were steering inward or outward of the cathode tips. We made an adjustment to the diode setup and were able to get two good shots.

To analyze the films, we scanned them and correlated them to a set of calibration films that were exposed to precise doses at the Gamma Irradiation Facility in Tech Area 5. A neural network machine learning algorithm was trained on the calibration films and used to predict the dose vs. distance along the films. A set of single energy dose response curves was simulated using MCNP6 and these curves were used to unfold the electron energy spectra from six of the films. For the current measurement, B-dots captured the differential current measurement through the pinholes and these signals were baseline corrected and integrated to produce current traces for each shot.

We found that the end-point energy of the electron beam spectral unfolds generally agrees with the end-point energy of the x-ray unfolds for standard brems shots. This was a good confirmation of the validity of technique. We found that the uncertainty in our measurements was no better than the uncertainty of an x-ray unfold, although using lessons learned we could certainty improve the fidelity of this measurement. We found that in general the electron beam energy cut-off was about 1.5-1.8 MeV, which is generally stated as the end-point energy of the source. We did find an example film that showed a cut-off energy above 2 MeV. It is difficult to say with certainty if this was real or caused by other scattering effects. The measured currents are in reasonable agreement with estimates of the current of a pinched beam filament, about 40-50 kA.

ACRONYMS AND DEFINITIONS

Abbreviation	Definition
AXIOM	An X-ray Intensity Operations Monitor
Brems (source)	Saturn's 3-ring bremsstrahlung x-ray source
CVR	Current viewing resistor
DAS (stack)	Differential absorption spectrometer
DAS	Data acquisition system
DDP	Depth-dose profile
GIF	Gamma Irradiation Facility
LDRD	Laboratory directed research and development
MCNP	Monte Carlo N-Particle transport code
MITL	Magnetically insulated transmission line
MTG	Marx trigger generator
NIST	National Institute of Standards and Technology
RCF	Radiochromic film
SMA	A radio-frequency coaxial connector
VVM	Vacuum voltage monitor

1. BACKGROUND

This section is intended to provide context for why we would like to measure the electron beam energy of the bremsstrahlung source on the Saturn accelerator. A brief description of Saturn and the 3-ring bremsstrahlung x-ray source (brems source) are given along with the motivation of why we would like to know the electron beam energy spectrum. We then provide a quick dive into the historical context of voltage measurements in the center section. We then describe the technique used in this work to measure the electron energy spectrum and its demonstrated use at the RITS-6 accelerator.

1.1. Motivation

The Saturn accelerator is a 36-line converging power flow pulsed power driver designed primarily to drive a 3-ring pinched beam diode as a bremsstrahlung x-ray source. The accelerator was commissioned in 1987 and has been operating ever since. The facility operates primarily as a production user radiation facility so the diagnostics near the load region are focused on the x-ray dose and dose-rate environments. There are few diagnostics in the center section of the machine, just three B-dots on each of two of the six vacuum transmission line levels. As the machine is run today, there is no measurement of the load voltage and although recently there have been V-dots installed in the A level magnetically insulated transmission line (MITL), these diagnostics are rarely connected and transformations assumptions are required to use them to calculate a load voltage.

This lack of load voltage diagnostics poses some problems when trying to model the machine operation and performance from a pulsed power standpoint. It has made it difficult to tune circuit models of the machine in order to make incremental improvements. Our main reason for undertaking this work was motivated through the AXIOM LDRD project (213089). AXIOM is time-resolved hard x-ray spectrometer designed specifically for Saturn's radiation environment. Two of the major design decisions involved choosing a filter set and an x-ray shielding geometry and both choices are dependent on what we believe the x-ray end point energy to be. In the absence of voltage measurements in the center section, we had to rely on x-ray spectral unfolds using the legacy differential absorption spectrometer (DAS) stack. We came to find out that there are huge uncertainties in this unfold so we endeavored to make a direct measurement of the energy spectrum of the electron beam so we could model the expected x-ray spectrum with higher fidelity.

1.2. 3-Ring bremsstrahlung x-ray source

Saturn's primary radiation source is the 3-ring bremsstrahlung x-ray source. It is a pinched beam diode which sends a high energy electron beam into a tantalum converter to produce bremsstrahlung radiation with a spectral end point energy of approximately 1.5-1.7 MeV. As the name suggests, there are three cathode rings that act as three independent radiation sources that combine to give the effect of a large planar source. The diodes themselves do not operate at the same voltage with the inner cathode being slightly lower than the middle and outer cathodes. This hasn't been measured experimentally but circuit simulations suggest it is the case. This experiment has been designed to attempt to make the first direct measurement of this difference.

1.2.1. Historical voltage measurements

A SAND report on Saturn shortly before it was commissioned contain a figure that suggest that vacuum voltage monitors (VVMs) were to be used in the center section [1]. These attach to the upper and lower cathodes through holes in the upper and lower anodes. Figure 12 from that report

is shown below. These voltage monitors are only mentioned in one sentence in the text of the report. A second report shortly after Saturn was commissioned used the exact sample figure of the center section but made no mention of the VVMs in the test of the report [2].

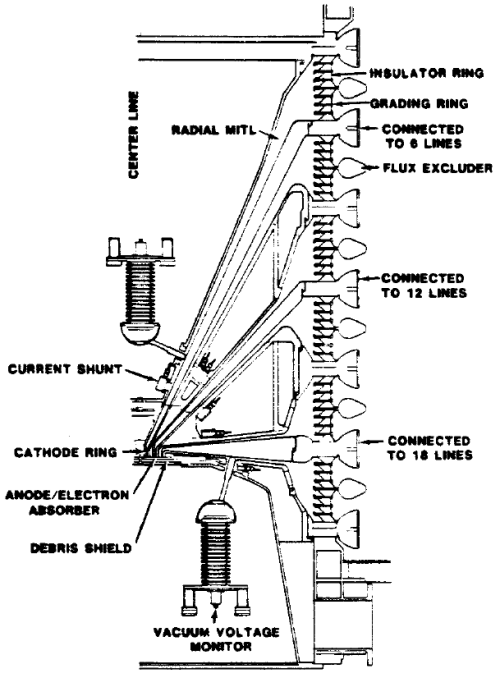

Figure 1-1. Diagram from Bloomquist et al. [1] showing vacuum voltage monitors in Saturn center section.

Hedemann et. al. published the first results characterizing the Saturn x-ray source [3]. It mentions the peak voltage of the accelerator of 2.0 MV with a reference that is only a private communication. There are no VVM measurements shown. The only measured data is dosimetry.

Other reports from that era such as the *Engineering Design of the Saturn Accelerator* [4] also include a diagram of the center section with no VVMs shown and no mention of them in the text. The VVMs are mentioned in the *Final Design Review Document for the Magnetically Insulated Transmission Line Module of Saturn* but only as part of the electrical criteria for the design [5]. They are never mentioned in the detailed meeting minutes through the rest of the document. Additionally, the *Saturn Baseline Document* which contains the detailed work breakdown structure (WBS) only indicates that "Provision will be made for voltage and current diagnostics at the vacuum insulator and in the vacuum convolutes" [6]. The lack of definition in the WBS and the lack of any measured voltage signals in subsequent SAND reports leads us to surmise that VVMs were left on the design table and even if they were used, it was on a limited basis.

1.3. Measuring particle beam energy using wedge technique

One technique for measuring the energy of a beam of directly ionizing particles is to measure its energy deposition in a solid material as a function of material depth when the beam is incident on the surface. This is most easily accomplished with charged particles such as electrons, protons, or other ions. This is easiest for protons or ions in that there is a well-known and fairly-well localized "Bragg peak" near the maximum range of the particle of a certain energy. The depth of the Bragg peak can be compared to look-up tables or models. Electrons do not have a well-defined Bragg peak

due to differences in the dE/dx values compared to ions where dE is the differential (collisional) energy loss in the material with differential thickness dx and also due to the fact that the electrons scatter widely in the material while ions scatter much less. Nevertheless, the physical process is similar. The resulting electron "depth-dose profile" (DDP) can be well correlated to the electron energy when monoenergetic. Some examples are shown in Figure 1-2. Even with a modest energy spread, an average energy can be related to the "R_{50}" depth or the depth at which the DDP is 50% of the peak dose [7]. Conversely if one knows the electron spectrum, angular divergence, and the presence of x-rays, one may accurately model the DDP to high precision as shown with an example in Figure 1-3 [8]. It is more difficult to go the other direction in that we measure the DDP but the spectrum is unknown.

One somewhat extreme example [9] of this is shown in Figure 1-4. The exact experiment is out of the scope of this report, but the key thing to know is there was an electron beam which was approximately mono-energetic at about 3 MeV and then some fraction of the electrons were accelerated to a maximum of about 3.875 MeV (as indicated by models and other measurements) which introduced a large spread to the overall electron spectrum. Since only the high-energy component of the electron spectrum is detected at larger depths, the 3.875 MeV electrons should be detected separately from the lower energy electrons. Indeed, the measured spectrum as shown in Figure 1-4 appears to agree well with a mono-energetic 3.875 MeV DDP at the same depth. Therefore, this measurement seems to indicate that even a DDP with a large energy spread can still indicate a peak energy. In large measure this motived the interest in performing a similar measurement at Saturn since a large energy spread is entirely expected. If we can measure the peak depth of electron penetration we can infer the peak *detectable* energy which constrains the x-ray peak spectrum and gives us some information on the Saturn diode voltage though other effects can modify the electron energy including plasma and beam effects, some of which *can* add or subtract energy.

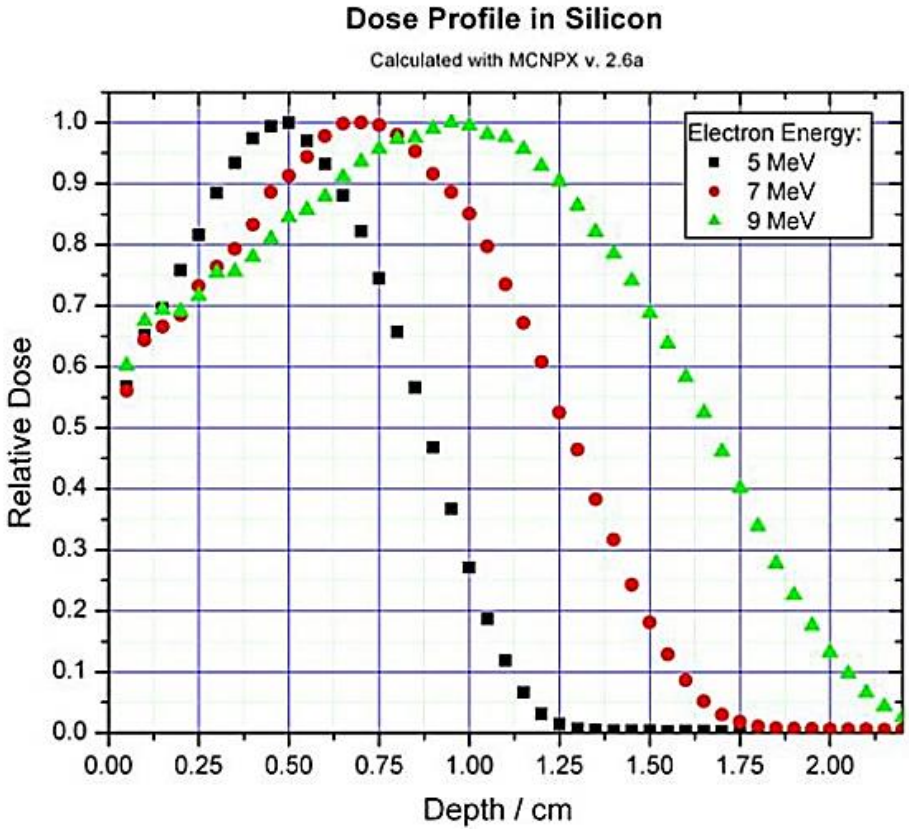

Figure 1-2. Example depth-dose-profiles in silicon for three different energies [9]. Each profile has been normalized to its own peak dose; generally peak dose decreases in amplitude as the energy increases.

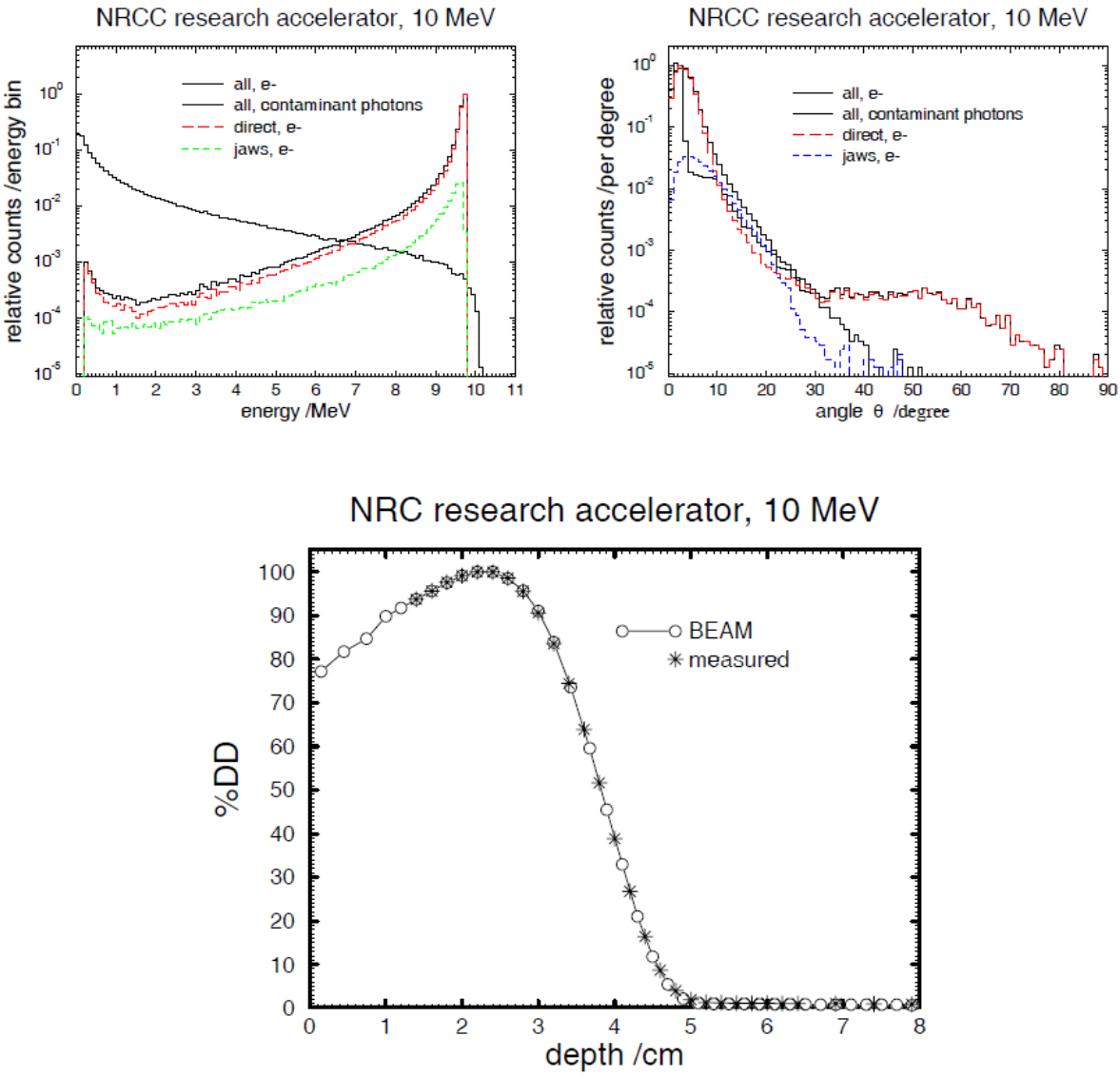

Figure 1-3. (Lower panel) Normalized DDP using the beam energy spectrum (upper-left) and angular divergence (upper-right) from Reference 8.

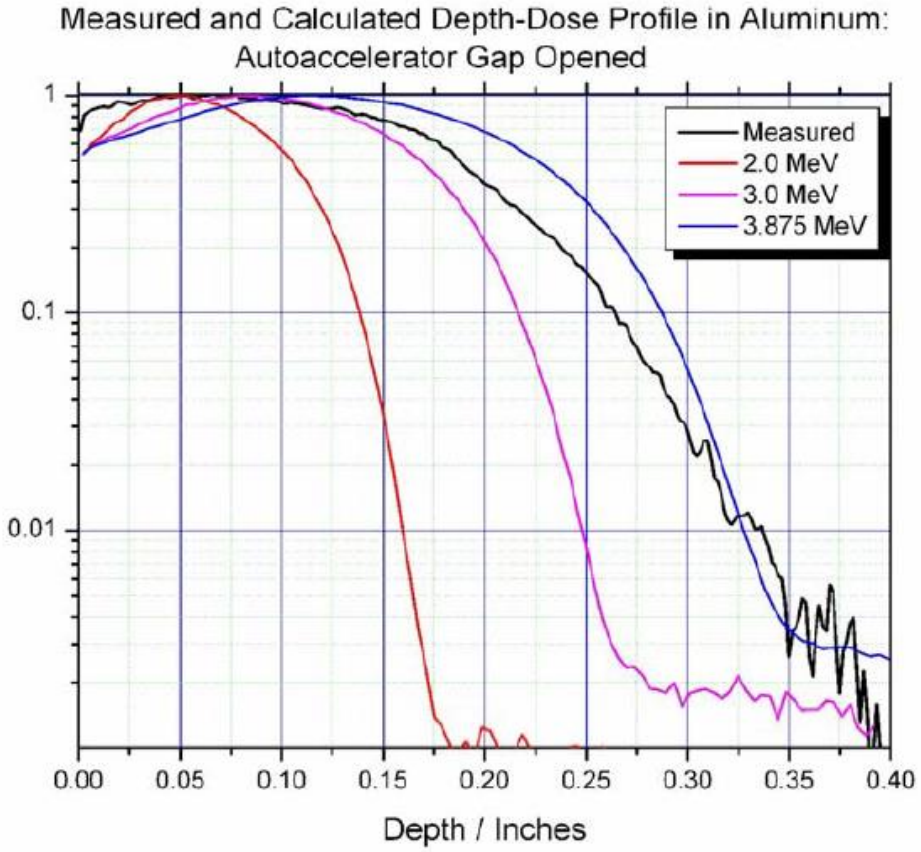

Figure 1-4. Measured and calculated DDP from Reference [9]. The purpose is to demonstrate that the measured electron maximum range at around 0.35 inches is close to the 3.875 MeV mono-energetic DDP showing that electrons with that energy is present.

1.3.1. Use of DDP for spectral information at RITS-6

RITS-6 [10] is an inductive voltage adder accelerator with a focus as a testbed for radiographic sources. There is a large-area diode (LAD) for general testing and this configuration was used [10] to make a DDP measurement. The end-point voltage of RITS-6 is well known since the voltage is a sum from the six accelerating cavities into the magnetically-insulated transmission line (MITL). Additionally, there is the potential for voltage oscillations to occur in the relatively large "dustbin" vacuum chamber around the diode region. The LAD can be set with an appropriate anode-cathode gap and cathode size to provide a mostly uniform electron beam on target with electron density (electrons/cm^2) within the dynamic range of the radiochromic film (RCF) used to measure the DDP.

The experimental geometry is shown in Figure 1-5. The RCF is sandwiched between two aluminum plates. The RCF is several inches long, perpendicular to the beam direction, about 2 inches wide, along the beam direction, and only a few hundred microns thick. Therefore, the long direction measures the beam profile (electron density) and the short direction measures the DDP. Since the RCF is so thin and the electrons have large angular deflections in the material, the dose deposition is dominated by the aluminum rather than the RCF (which is essentially a plastic film), the DDP material is considered aluminum only.

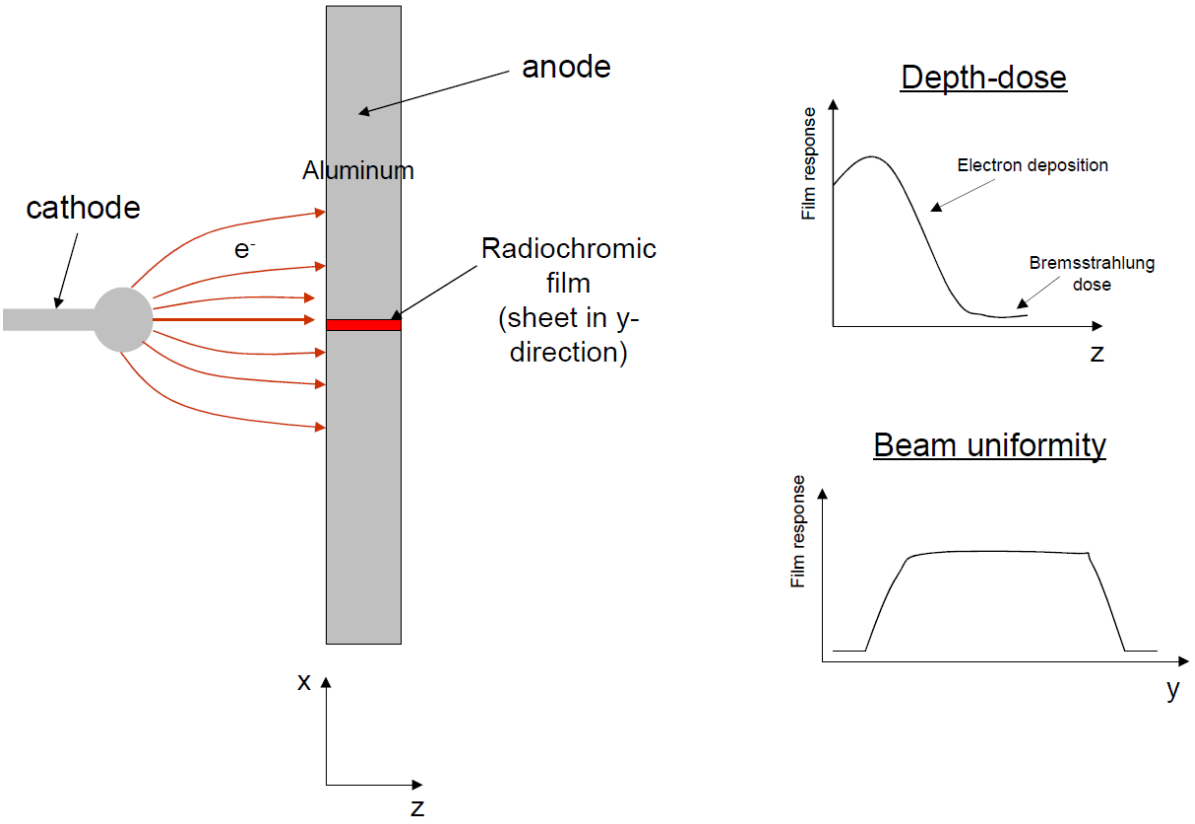

Figure 1-5. RITS-6 DDP measurement geometry and diagram of LAD indicating approximate electron trajectories (left). Simplified sketches of expected measurements in the two dimensions of the RCF plane.

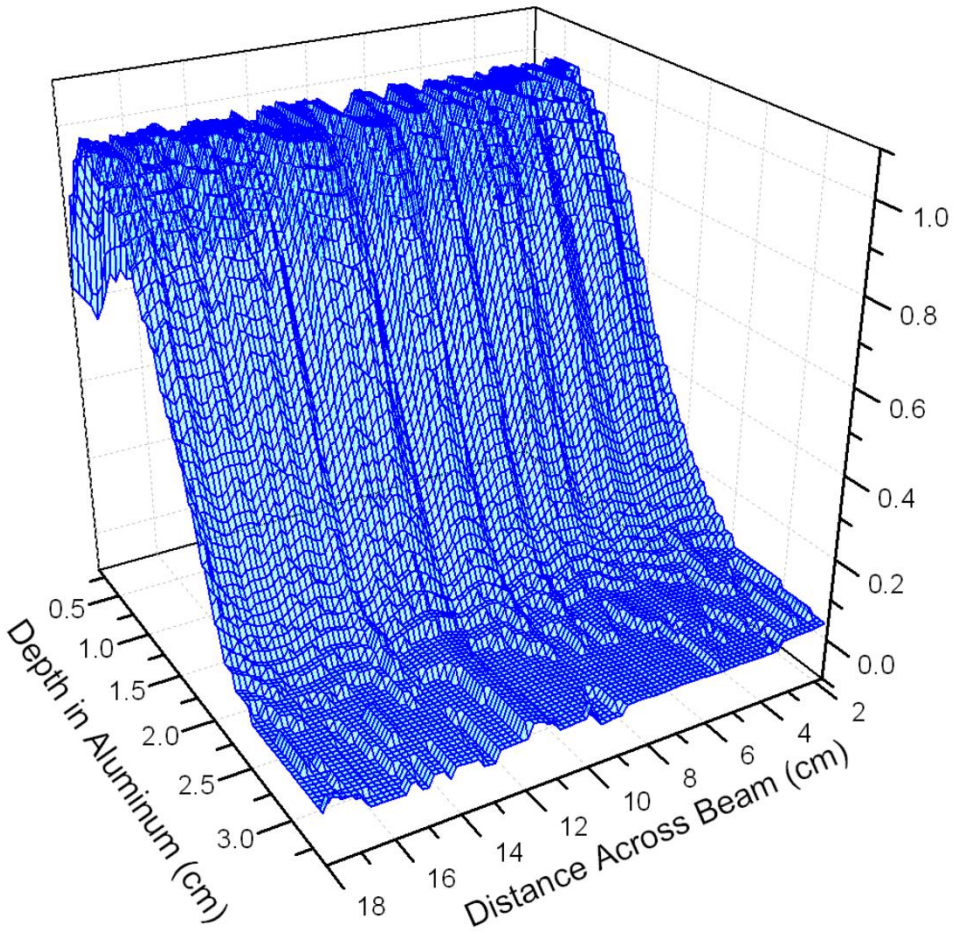

Figure 1-6. Example RITS-6 measured DDP. The original data showed < 20% variation in beam dose profile across the beam but this variation largely goes away if point-by-point DDP normalization is done across the beam.

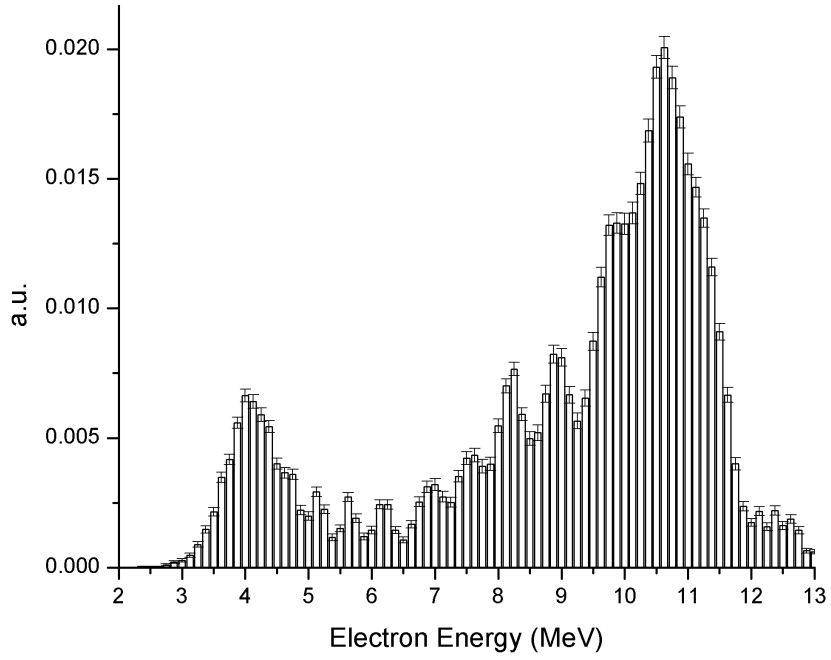

Figure 1-7. Unfolded electron spectrum from a DDP on a RITS-6 shot (not necessarily the same as the DPP from the last figure). The error bars indicate a per-bin standard deviation after averaging the unfolds from individual DDPs across the beam like that shown in the previous figure.

2. WEDGE DESIGN

This section describes the design of the wedges used to measure the Saturn electron energy spectrum. We undertook MCNP simulations to guide our design of the wedge geometry. The properties of the radiochromic films we chose as well as how they were calibrated are discussed.

The geometry of the DDP for Saturn needs to look much different than that used for RITS-6 for the main reason that it is impractical to put the RCF parallel to the beam direction due to the much shorter ranges considered. The projected range for 2.0 MeV (1.0 MeV) is 4.5 mm (2.0 mm) in aluminum. An alternative geometry is that of a "wedge" where the RCF is sandwiched between two pieces of aluminum, the top being a thin triangular wedge so that the depth of the aluminum from the top (beam incident) surface increases along the RCF length. This is indicated in Figure 2-1. Therefore, the dose along the length is equivalent to dose-versus-depth in aluminum. A dose profile requires knowledge about the surface electron fluence or for the beam to be uniform (or very slowly varying). Ideally, an RCF on the surface would measure the incident beam. Provision was made to attempt to create the uniform beam conditions which are described later. The two-dimensional RCF film allows profile measurement transverse to the DDP (out of the plane of Figure 2-1) which gives some information on dose profile shape since the beam profile should have a large degree of circular symmetry.

The wedge angle of 7.4° was calculated by choosing a somewhat arbitrary RCF length of about 1.5" and setting the aluminum thickness at the planned beam axis equal to the electron range of 1.5 MeV which is close to the expected value. We did not expect our measurement to be strongly dependent on these choices.

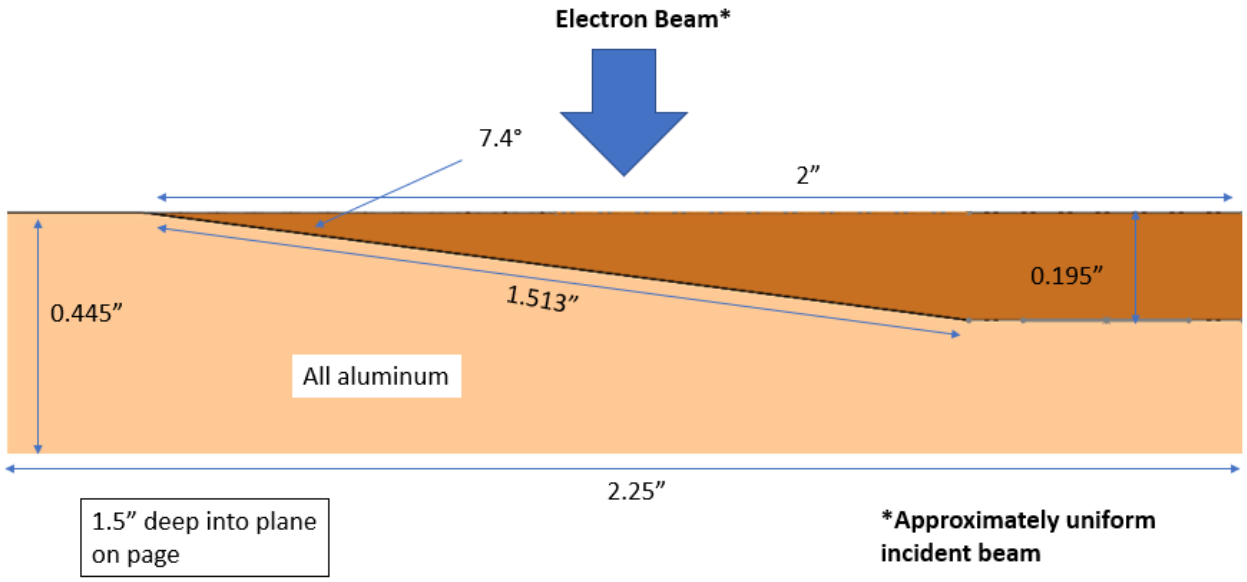

Figure 2-1. Dimensions of the Webb's Wedges. The RCF is sandwiched between the two aluminum parts (two different colors) on the slope.

Since the current density was highly unknown at the onset of these experiments (especially the planning stage) and the dynamic range of the DDP could be quite high (>100x), we chose to use a stack of two types of RCF on most of the wedges [12, 13]. The resulting range of the combined films (the sensitivities overlap) would be < 10 Gy to > 100 kGy. Schematically the setup, including

distance from the anode tantalum foil, is shown in Figure 2-2. This combined assembly constitutes (an example of) what we have called "Webb's Wedges".

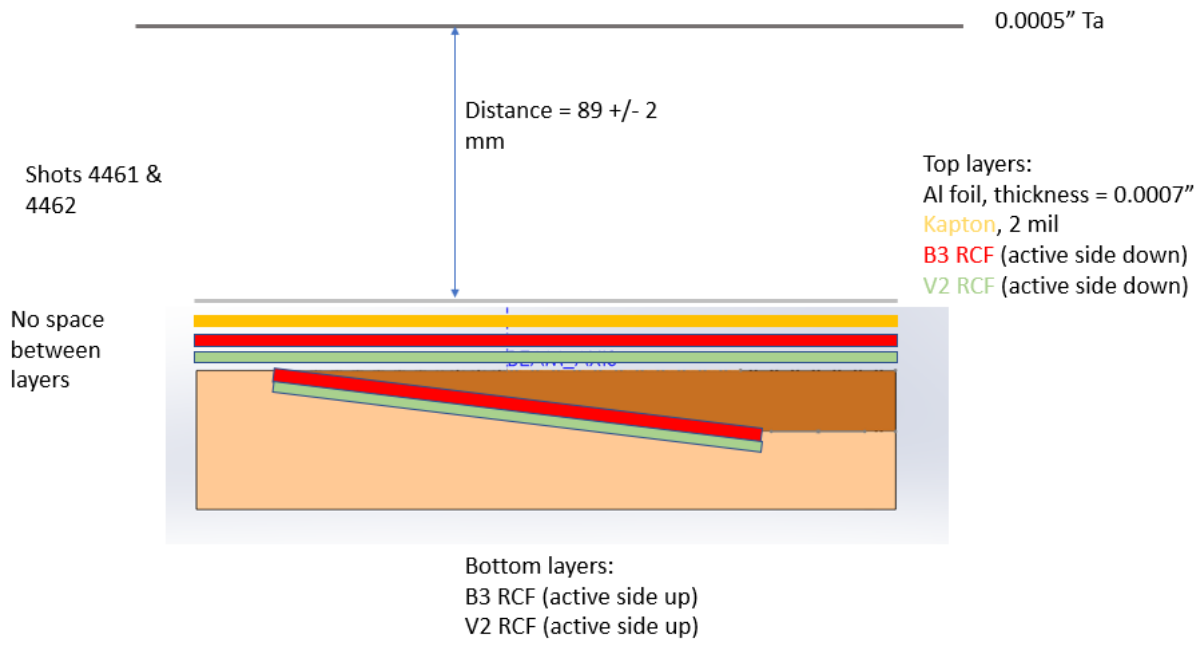

Figure 2-2. Diagram of the Webb's Wedges DDP showing the placement of the RCF and other layers with respect to the tantalum anode foil. The beam aperture is not shown.

2.1. MCNP simulations

The analysis of the Webb's Wedges DDP requires (at least) two dimensional simulations of the RCF response(s) using the accurate (as-made) dimensions since we were not sure if a one-dimensional equivalent would give the same result. For instance, deviation from the 7.4° angle will affect the effective aluminum thickness. We used MCNP 6.1 [14] to calculate the depth-dose profile in each of the RCF layers. MCNP has been shown to have good comparison with other Monte Carlo codes [15].

2.1.1. Simulation setup

An example input file is given in Appendix C. The input "beam" is rectangular but is only required to "over-fill" the tally region of the film in the two lateral dimension transverse to the beam direction so that there are no edge-effects. Therefore, the simulation is effectively two dimensional with the out-of-page dimension essentially playing no role. A Type 3 mesh tally was chosen which allows a user-defined dose mesh with a prescribed spatial resolution. In this case, the mesh was 0.01 cm wide along the length of the film. The number of particles run in the simulation (100 million) resulting in a per-pixel standard deviation of less than 0.4% over the electron deposition region. For reference, the simulation takes on the order of only 900 seconds of CPU time to achieve this precision, so it is easy and relatively quick to make a large number of simulations using different input electron energies. Also, the scaling is essentially arbitrary except that the beam fluence must be kept constant for all beam energies.

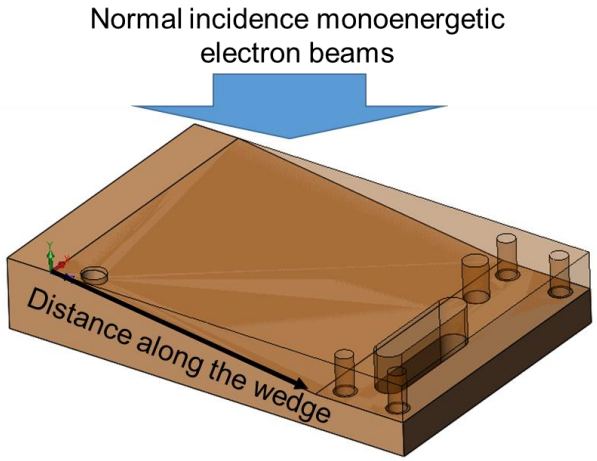

Figure 2-3. General diagram of the MCNP simulation.

One difference which may affect the result when comparing the simulation and experiment is that the MCNP simulation uses a "parallel" beam which has zero beam angular divergence. In reality the Saturn beam is expected to have some beam divergence since it originates from a small aperture and angular spread will result from scatter from the tantalum, space-charge repulsion, and whatever beam angle the electrons had in the A-K gap of the diode.

2.1.2. Results

A library of Webb's Wedges DDP has been compiled from 0.2 MeV to 2.2 MeV and are shown in Figure 2-4. These curves were used in the spectral unfolding effort described in section 5.1.

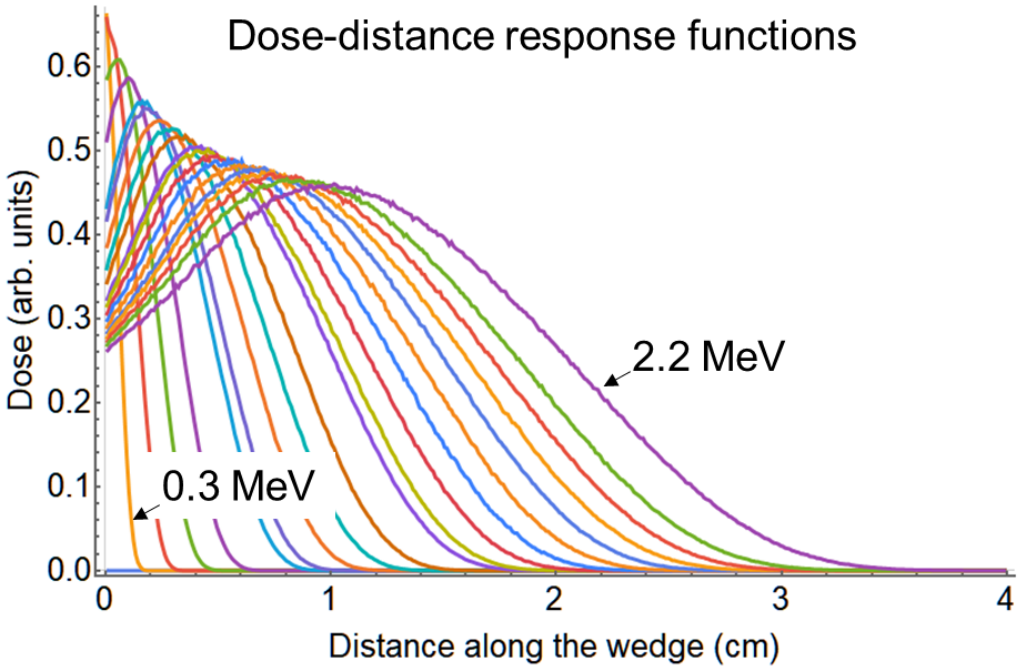

Figure 2-4. Unnormalized dose profiles of the Webb's Wedges used for the spectral unfold and comparison with the maximum energy at maximum depth measured for the electron DDP.

2.2. Radiochromic film selection

Radiochromic films contain pigments which are sensitive to total absorbed dose. This means they change color when exposed to radiation. We chose to use two different films to cover a wider range of possible doses. One of the films, GafChromic HD-V2 film manufactured by Ashland Advanced Materials (called V2 film throughout this report), is sensitive to doses over a dynamic range of approximately 10 Gy to 1 kGy [11]. It is a yellow film that changes color to green and eventually darkens to completely black with increasing dose. It consists of a 12 micron active layer on top of 97 micron polyester substrate modeled as $C_{10}H_8O_4$. It has a density of 1.38 g/cm^2.

The other film used is called B3 produced by GEX Corporation and is sensitive to a wider range stated by the manufacturer as between 300 Gy and 160 kGy [12]. It starts off clear and becomes increasingly pink with increased dose until it saturates as a dark shade of magenta. The film has an 18 micron active layer on top of a 48 micron backer layer that can be approximately modeled at C_2H_4. It has a density of 1.39 g/cm^2.

For both films the region of highest sensitivity is on the low dose side of their ranges. The change in coloration is rapid and easily spotted for small doses. On the high dose end of their ranges, only image processing analysis can differentiate the different shades of green or pink.

2.2.1. Calibration of radiochromic films

The radiochromic films were calibrated at the Gamma Irradiation Facility in Tech Area 5 using the Co-60 source. The facility has NIST traceable dosimetry to precisely determine the fluence applied to our samples. The results of the calibration are shown in Figure 2-5. The greenish samples are V2 film while the pinkish samples are B3. It should be noted that the two calibrations were not done simultaneously even though the V2 and B3 films share two of the same dose calibration points.

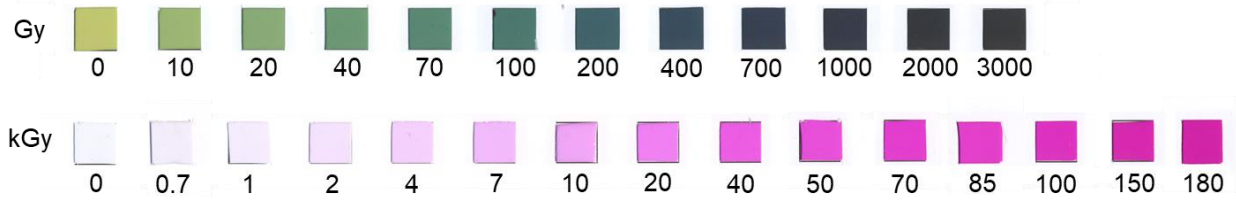

Figure 2-5. Calibration film swatches for the V2 (yellow/green) and B3 (white/pink) films. The values listed for V2 are in units of Gray while the B3 film calibrations have units of kiloGray.

3. EXPERIMENT DESIGN

This section describes the concept and design of the Webb's Wedges experiment. The changes to the standard load configuration are first discussed. We then discuss the thought process behind mounting and positioning the wedges. Finally, the section concludes with the design of the current monitors and our calibration process.

3.1. Conceptual design

The concept of this experiment is to extract a small portion of the electrons being emitted from the cathode tips of Saturn's 3-ring bremsstrahlung diode and allow them to expand through space charge effects before depositing into the wedge. The intent was to not change the pulsed power of the diode so that it replicated the normal conditions of the brems source as much as possible. We used the same anode material so the ion return current and gap closure dynamics would remain the same, but the foil was thinner (0.5 mil compared to 5 mil) so that the beam would scatter without losing much energy. The scattering foil was also intended to broaden the beam to prevent saturation or destruction of the radiochromic films and provide, as much as possible, a uniform surface fluence on the top of the wedge. Figure 3-1 shows a sliced 3-D model of the setup.

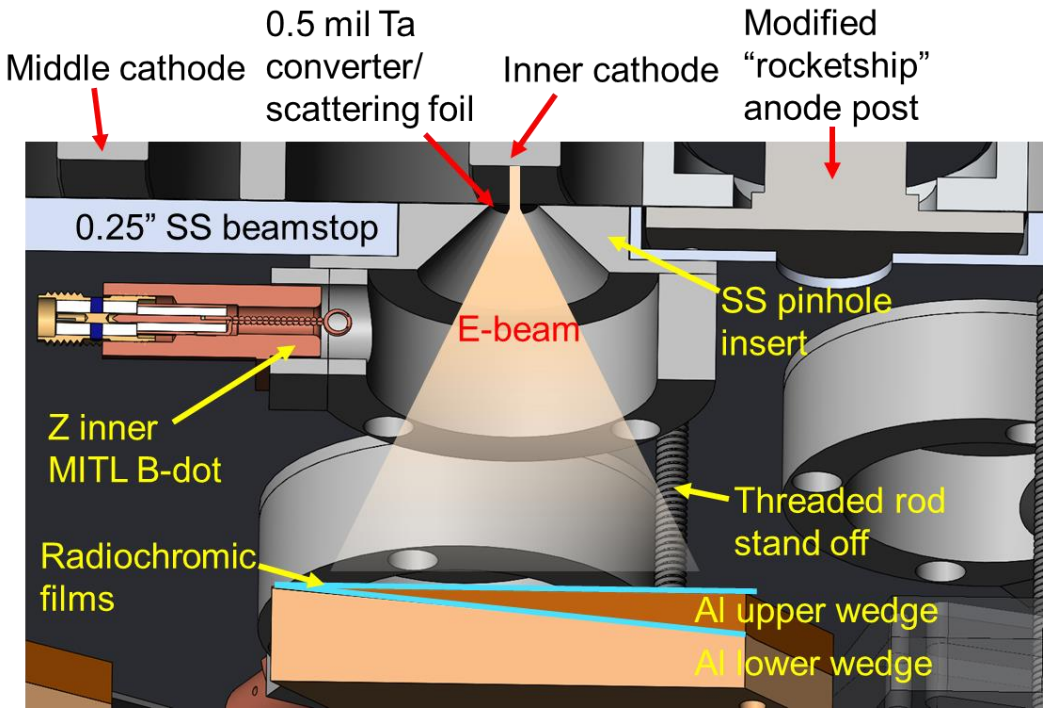

Figure 3-1. Sliced model of the Webb's Wedges experiment setup.

The extracted beam propagated through a stainless steel pinhole insert that was mounted a 0.25" stainless steel beam-stop, replacing the 0.063" aluminum beam-stop normally used. We wanted our beam-stop to be total stopping for the electrons and be mechanically strong enough to absorb the energy of the electron beam not being extracted without deforming. Our tantalum anode foil was stretched between the standard lower anode diode feed and a new stretcher ring with notches milled out in four azimuthal locations where the beam-stop is mounted. This is shown in Figure 3-2. The

beam-stop mounts into the stretcher ring such that is no gap between the anode and the beam-stop as there is in the standard configuration.

At the time of this experiment, the pinch bolt had a large screw on both ends. As originally designed, one end screws inside the upper anode tip "rocketship", securing the anode foil to the lower aluminum cup. The other side holds the vacuum window in the brems dome. Because we are hanging our diagnostics off the beam-stop, we couldn't use the normal brems dome and instead used the flat-top dome. The lower screw on the pinch bolt was cut off because it wasn't needed, and it interfered with our wedges. This was the first example of the what became "decoupled" mode, eventually the standard configuration of the diode.

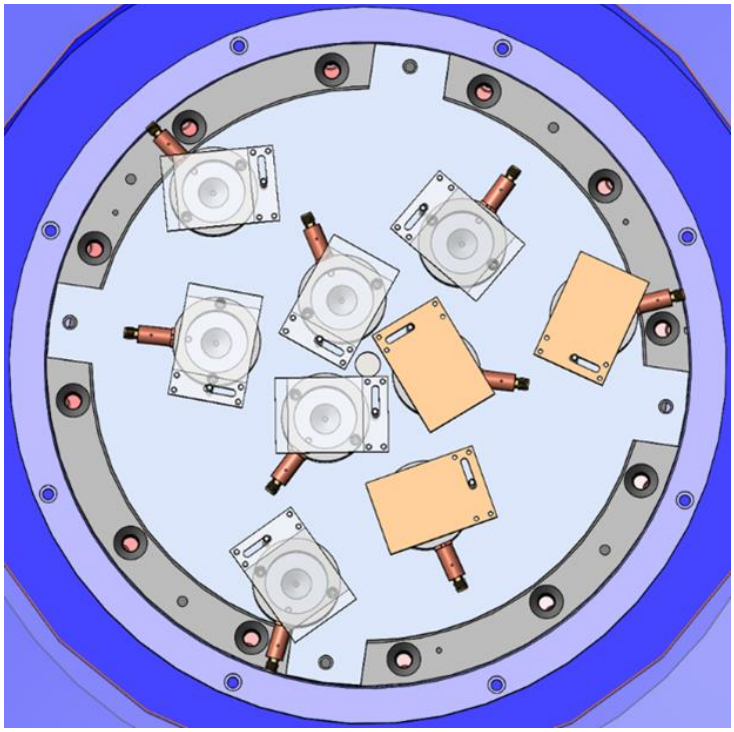

Figure 3-2. View of the Solidworks model looking up at the diagnostics mounted on the beam-stop. Some of the wedges are transparent to show the position of the pinhole axis on the wedges.

3.2. Source installation procedure

The MITLs are loaded, the diode feed hardware is mounted, and concentricity as performed as normal. The anode and cathode tips are installed and the A-K gaps of the cathode tips are set as usual. At that point, the installation procedure deviates from the standard install.

The rocketship is screwed into the upper anode. No spacer rings are used and the aluminum cup is press fit onto the brass rocketship. The 0.5 mil tantalum foil is gently placed up and stretched on the lower anode feed using our modified stretcher ring. The pinch bolt was gently threaded into the rocketship until it made contact with the foil but before twisting the foil.

All wedges on the beam-stop were mounted and positioned ahead of installation on a benchtop. The beam-stop was mounted onto the stretcher ring. The B-dot cables were then connected and routed

down the underside of the lower anode using pieces of copper tape to hold them in place to the lower vacuum feedthrough port. A loaded standard DAS stack was placed in the middle of the vacuum window on top of the flat-top dome and the dome was mounted. The cables on the air-side of the feedthrough were then connected through the Saturn Test Stand and routed into the user screen room.

3.3. Webb's Wedges positioning

The beam-stop was designed so that the wedges could be positioned with three wedges per cathode ring without interferences in either the wedges themselves or the cable routing. Figure 3-2 shows how this was achieved with the wedges mounted at angles relative to each other. The slot in the wedge allowed us the flexibility to position the wedge either on centerline of the pinhole or off axis of the pinhole if the fluence was found to be too high and was saturating the radiochromic film. If that happened, it was thought then that we could just catch the edge of the expanding beam and avoid saturation.

3.4. Current monitors

The current monitor used on this experiment are Z inner MITL B-dots. We were able to get a handful of them for our experiment. The B-dots are the double looped variety meaning they are more sensitive than the single looped variety used more often at Z. The B-dot loop is oriented to see the azimuthal magnetic field of the electron beam which was expected to be coaxial to the aluminum ring the B-dot is mounted in.

3.4.1. B-dot calibration scheme

The calibration was performed in Jim Moore's lab in building 981, using the same pulser used to calibrate the B-dots for Z experiments. The setup used a current-viewing resistor (CVR) as the calibration reference. The pulser has a ~100 ns rise time with a current pulse shape roughly equivalent to the Z load current pulse. For these time scales, the B-dot operates in a *differential* mode in that the signal is proportional to the dI/dt of the current, I, of the current running in the center of the ring. While more sophisticated analytical models exist [16], for these times scales and desired precision, the measured current is the integral of the B-dot voltage V_B:

$$I_{beam}(t) = \frac{1}{M}\int_0^t V_B \, dt$$

M is the mutual inductance of the B-dot to the beam. Therefore, we calibrate the $1/M$ term using the CVR as the beam current stand-in. An example calibration is shown in Figure 3-3. Two values are returned from an automated analysis routine: the calibration value (effectively the $1/M$ term above) in Amperes/(Volt·seconds) and the peak raw b-dot signal in units of Volts/second/Ampere (this is approximately the inverse of the calibration value) which is an estimate of the peak measured voltage based on an expected or estimated dI/dt which can be very useful in setting oscilloscope volts per division vertical scale. In the case of the example in Figure 3-3, the values are 3.81×10^{10} (A/(V·s) and 2.7×10^{-11} (V/s/A) respectively. All the B-dots used on the Webb's wedges experiment were calibrated using this procedure and used the same CVR.

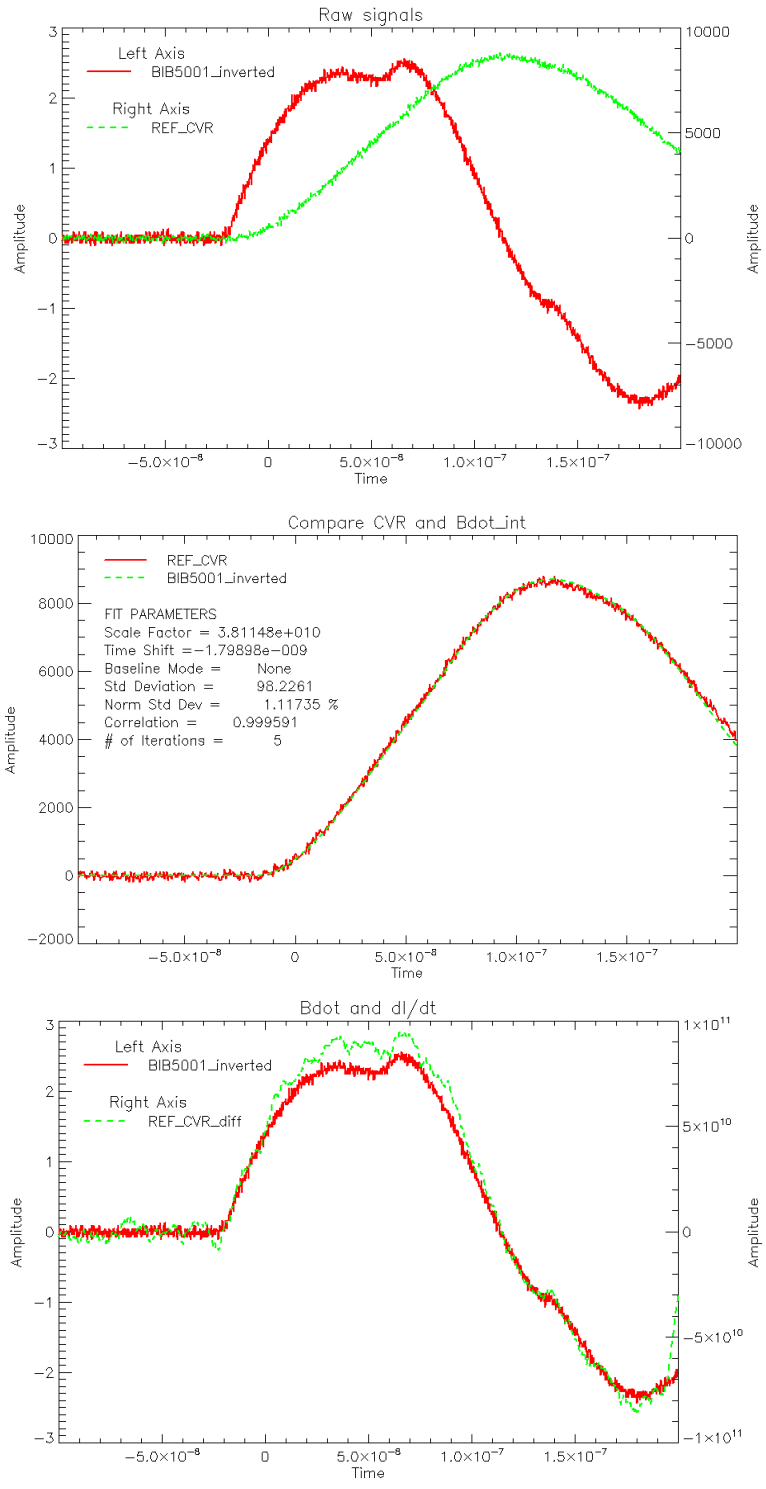

Figure 3-3. Top: Raw signals for the B-dot calibration with the CVR and B-dot. Middle: After integrating the B-dot signal, the result is scaled to the CVR. Bottom: The CVR is differentiated and the original B-dot signal is scaled to that result.

4. EXPERIMENT RESULTS

This section describes the experiment results and is broken down by shot number. For each shot, the specific changes to the setup are first described. Then the post-shot results are shown including the machine performance, a look at the post-shot hardware, and then a description of the B-dot signals and radiochromic films. The detailed analysis of the films and B-dot signals is made in Section 5.

4.1. Three shot series

We had one week scheduled for this experiment which meant four was the maximum plausible number of shots. Therefore, we planned for four shots by ordering that amount of hardware. It is always very ambitious to get all of the shots planned given the uncertainties in doing something new so we were pleased to get through three shots. In fact, we ended up using some of our fourth shot hardware on the third shot to try to mitigate an issue with debris.

4.1.1. Shot 4460 (First shot)

Because this experiment is intended to operate the same as the normal bremsstrahlung source, we did request any changes to the usual setup until it came time to mount the tantalum anode and beam-stop. We then connected the B-dot and noise channel cabling and used the flat-top dome instead of the normal brems dome. We also placed a standard DAS stack on top of the vacuum window.

4.1.1.1. Setup

For the first shot, we used an assortment of pinhole sizes to first figure out what would work. We were uncertain about the fluence we would get from the pinhole, the uniformity of that fluence across the wedges and which films would provide the best data, i.e. have good dynamic range but not saturate. We chose to use the same approximate working distance for all wedges which we continued to do through all shots. Each wedge had a single sheet of B3 and V2 radiochromic film sandwiched inside the wedge and the same on the top surface with an aluminum foil cover sheet to protect from debris.

We used the B-dots that showed the best behavior during calibration. They were connected through the Saturn Test Stand into the user screen room. There were attenuators on the patch panel into the screen room. We used 5x attenuators for all B-dots while the scopes themselves were set to the full scale. Again, we weren't sure exactly what we were going to see from the B-dots because there were large uncertainties in the amount of current we may extract through the pinholes. Each B-dot was also connected to two scope channels, one set at 5 volts per division (V/div) and the other at a more sensitive 1 V/div. We had two noise channels that had SMA shorts attached on the ends. Those cables were positioned near the B-dots on the diagnostic plate, taped in place near the outer B-dots. They used 20x attenuators at the user screen room bulkhead.

Table 4-1. Diagnostic setup for shot 4460

Signal Name	Detector	External Attenuation	Pinhole ø[1] (mm)	Distance[2] (mm)	Film Types
BD_INNER_1A BD_INNER_1B	B-dot 03	5x	4.06	88.8	B3/V2
BD_INNER_2A	B-dot 06	5x	5.08	89.5	B3/V2

Signal Name	Detector	External Attenuation	Pinhole ø[1] (mm)	Distance[2] (mm)	Film Types
BD_INNER_2B					
BD_INNER_3A BD_INNER_3B	B-dot 07	5x	6.10	89.2	B3/V2
BD_MID_1A BD_MID_1B	B-dot 09	5x	4.06	89.7	B3/V2
BD_MID_2A BD_MID_2B	B-dot 11	5x	5.08	89.3	B3/V2
BD_MID_3A BD_MID_3B	B-dot 12	5x	6.10	89.8	B3/V2
BD_OUTER_1A BD_OUTER_1B	B-dot 15	5x	4.06	89.7	B3/V2
BD_OUTER_2A BD_OUTER_2B	B-dot 16	5x	5.08	88.3	B3/V2
BD_OUTER_3A BD_OUTER_3B	B-dot 18	5x	6.10	88.6	B3/V2
NOISE_1	SMA short	20x	N/A	N/A	N/A
NOISE_2	SMA short	20x	N/A	N/A	N/A

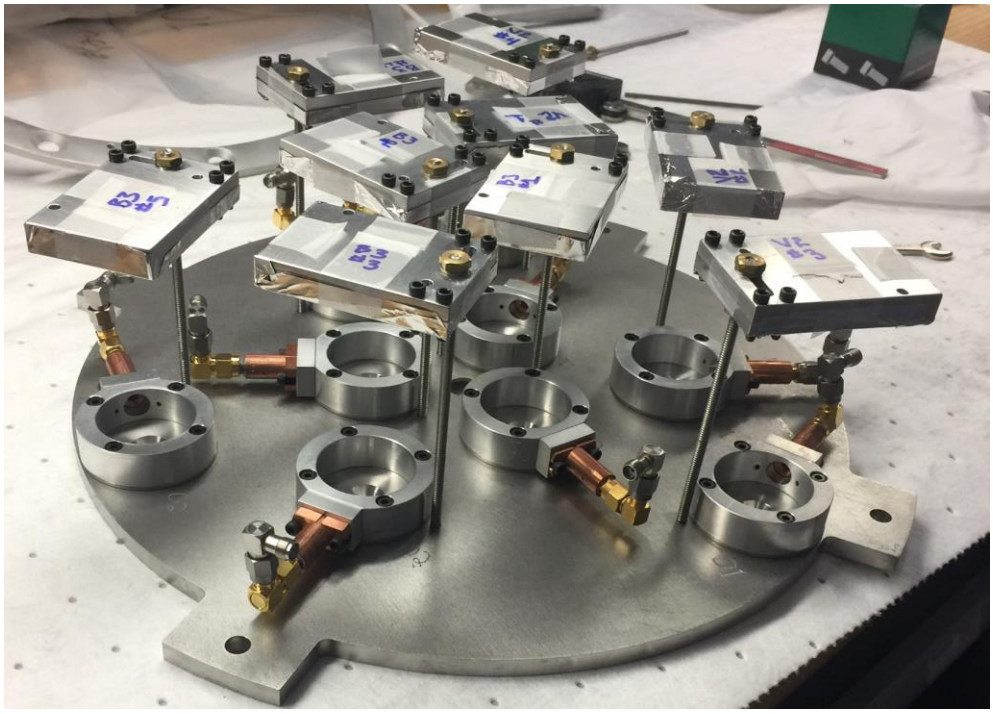

Figure 4-1. Beam-stop diagnostic plate for shot 4460.

4.1.1.2. Machine performance

Due to problems with line 28, that Marx was eventually bussed out leaving us to shoot 35 lines. The spreads on the MTGs were not very good, about 41 ns first-to-last. The target is for this number to be <25 ns. Experience has shown that while it is possible to get a decent shot after bussing out a line it is significantly less likely to occur.

4.1.1.3. Hardware autopsy and the debris problem

When we first inspected the hardware after the shot, we were surprised by the amount of destruction to the beam-stop and wedges. Figure 4-2 shows the underside of the beam-stop with large rings of spall damage opposite the cathode tips. Figure 4-3 shows this up close with the B-dots still attached. The pinholes themselves also spalled. This intense debris field caused numerous bullets to shred the top films on the wedges, shown in Figure 4-4. The impact was intense enough to bend some of the threaded rods holding the wedges and even strip out some of the threads.

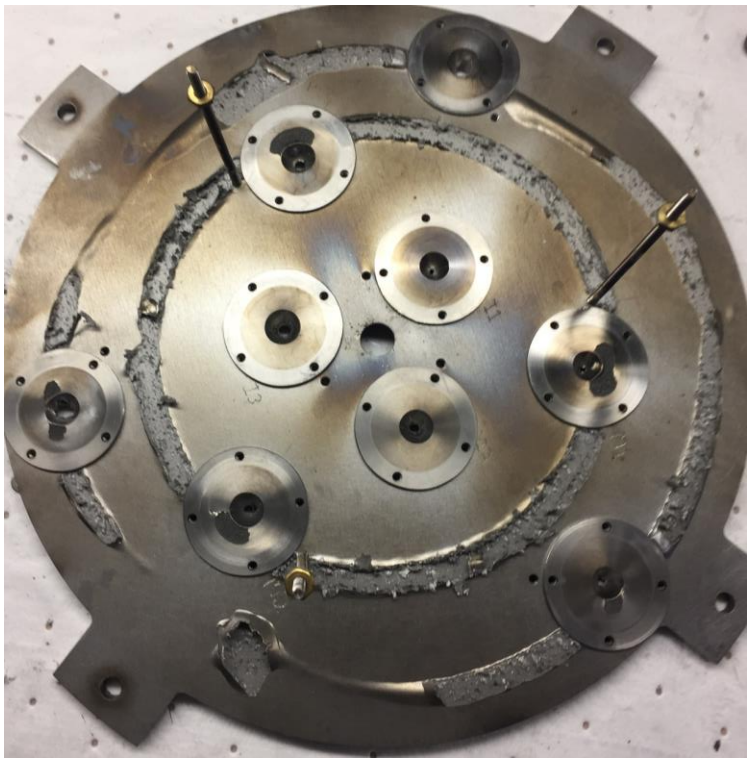

Figure 4-2. The backside of the beam-stop showing spall damage.

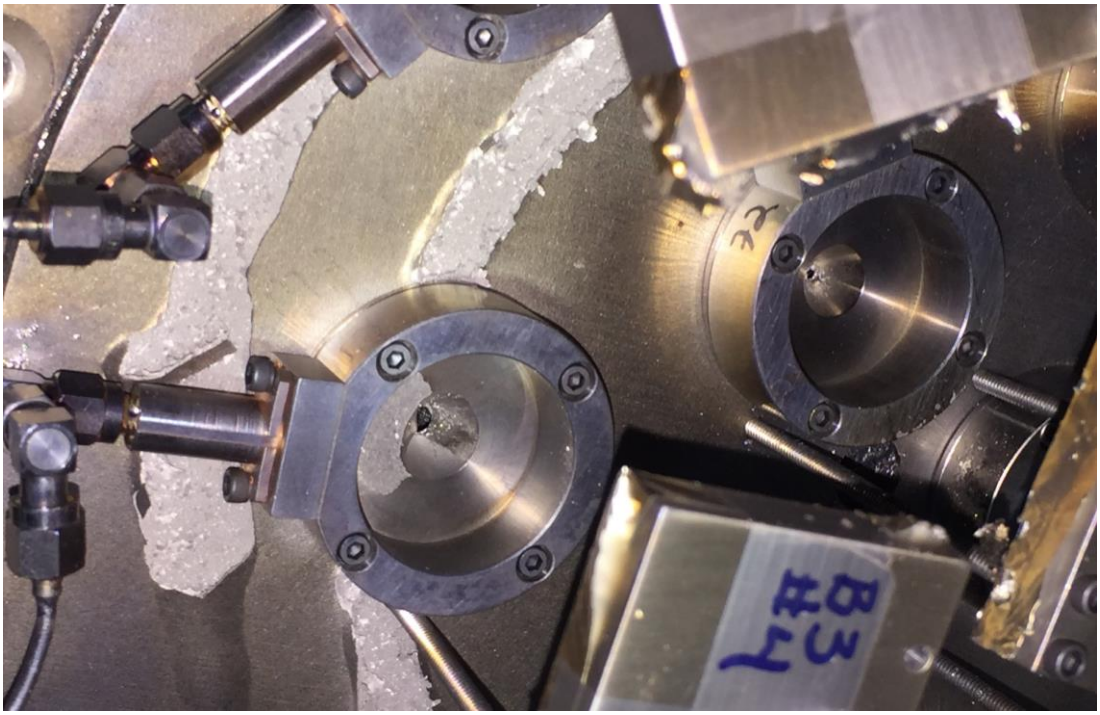

Figure 4-3. Detail photo of post-shot spalling of the beam-stop and pinholes.

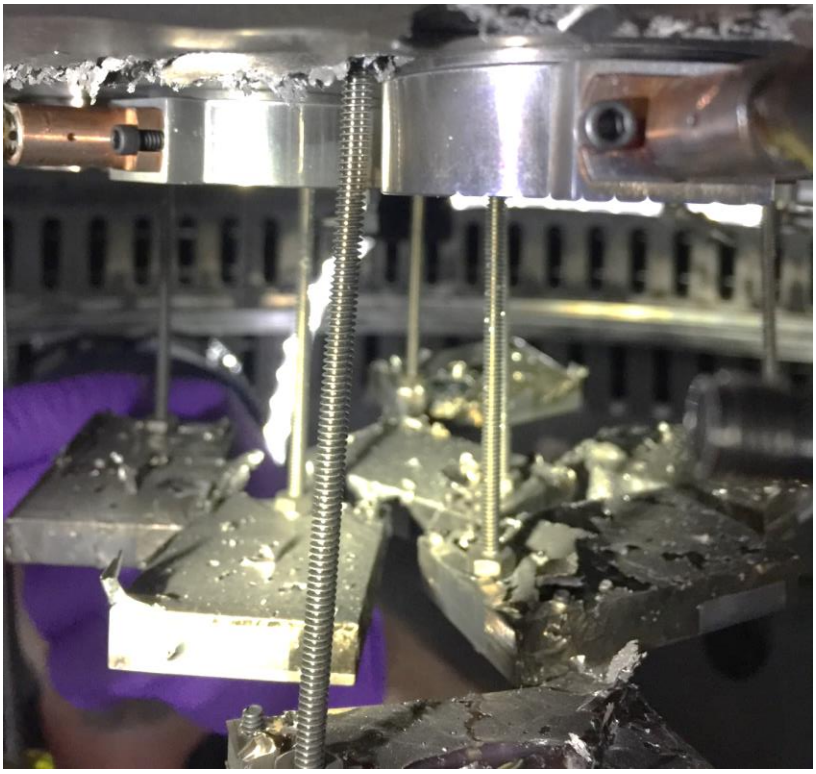

Figure 4-4. Photo showing the top surface of the wedges, films shredded by debris.

A larger problem than the debris is that the electron beam did not appear to go directly down through the pinholes. It was known that the beam can walk around on the anode but it was thought that during peak power the beam is fairly centered on the cathode tips. The burn on the beam-stop in Figure 4-5 showed this is not the case. The inner cathode burn was not even visible. The middle cathode burn seemed to have ridden the outer edge of the cathode tip, even projecting at an outward angle from the tip. The dramatic ring of melted steel on the top surface of the beam-stop (known colloquially as the "burn") was azimuthally uniform and fairly uniform in depth. There was evidence of a waviness in the azimuthal profile of the burn meaning that as expected, the Saturn electron beams are a series of pinches around the circumference of each cathode. This is in agreement with pinhole camera imaging on normal radiation production shots.

The outer cathode had a strange burn pattern. In some azimuths it was strong, uniformly deep and basically centered under the tip. In other locations it seemed to either walk to the inner or outer radius of the tip with varying intensity. The beams walking around the anode foil presented us with a problem that we solved on the second shot with a small change in the setup.

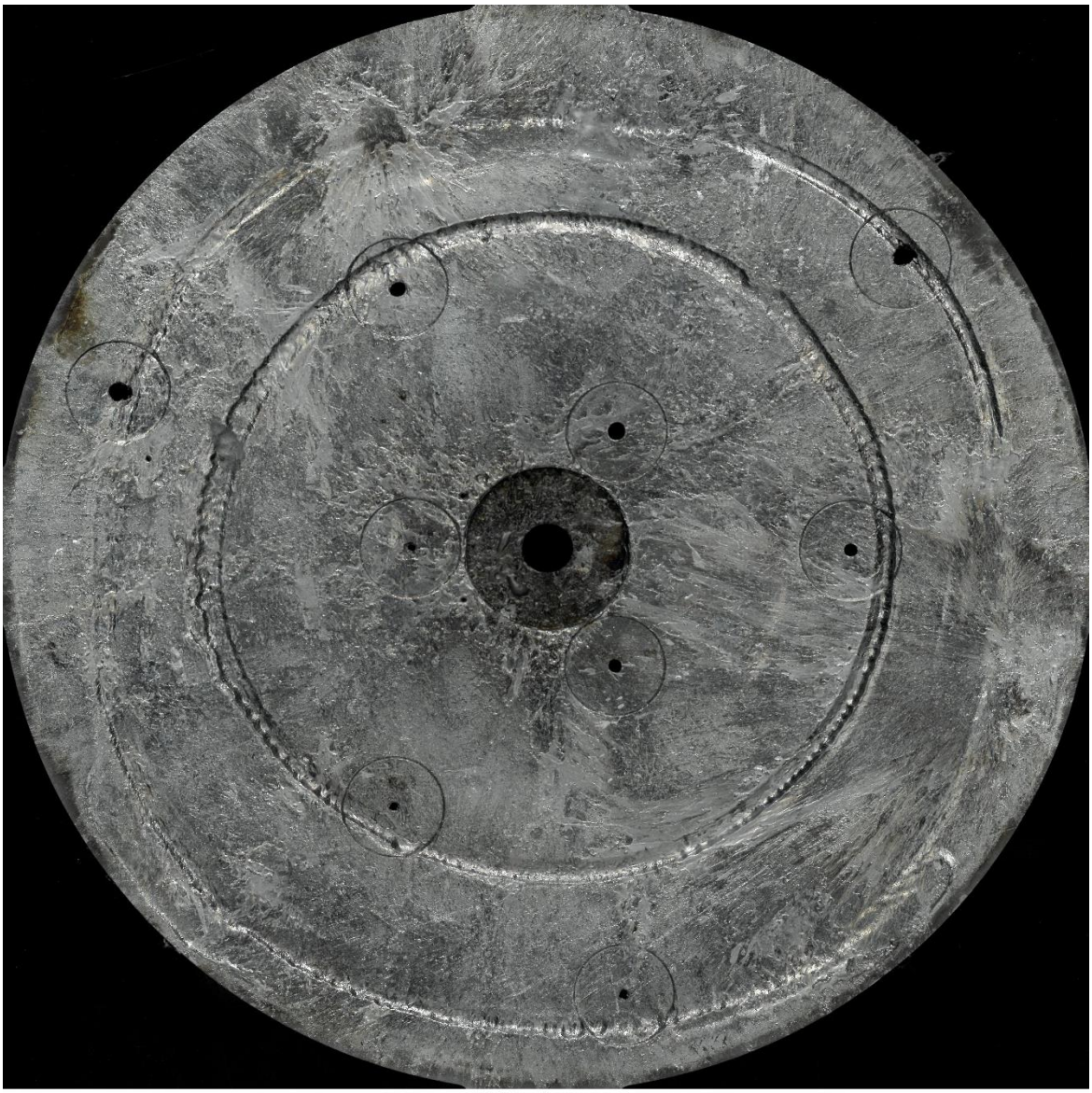

Figure 4-5. The beam-stop from shot 4460.

4.1.1.4. B-dot signals

The B-dot signals were collected via oscilloscopes operated via main Saturn DAS. That means they are all on the common control/monitor time base. The raw differential signals were processed using methodology detailed in Appendix A. The traces plotted in Figure 4-6 show the resulting processed currents measured by each B-dot. A heroic effort was made to manually find the baseline and subtract it such that the integrated signals came back to a near-zero baseline value. This technique resulted in an estimated error in the current of approximately 500 A meaning that for some of the pinholes, the error is a significant fraction of the peak current. This was due the peak e-beam current not passing through the pinholes as seen in the beam-stop burn, meaning that these signals do not represent the full pinch current.

The signals are named as "INNER", "MID" and "OUTER", representing the upper cathode, middle cathode, and lower cathode, respectively. The number is an arbitrary designation of the

azimuthal position but its orientation relative to the cardinal directions was not tracked. The signal for BD_INNER_1 is especially troubling because the positive-going initial pulse is real in the data. No amount of baseline correcting can eliminate it. The origin of this peak is unknown and does not show up in any other signals.

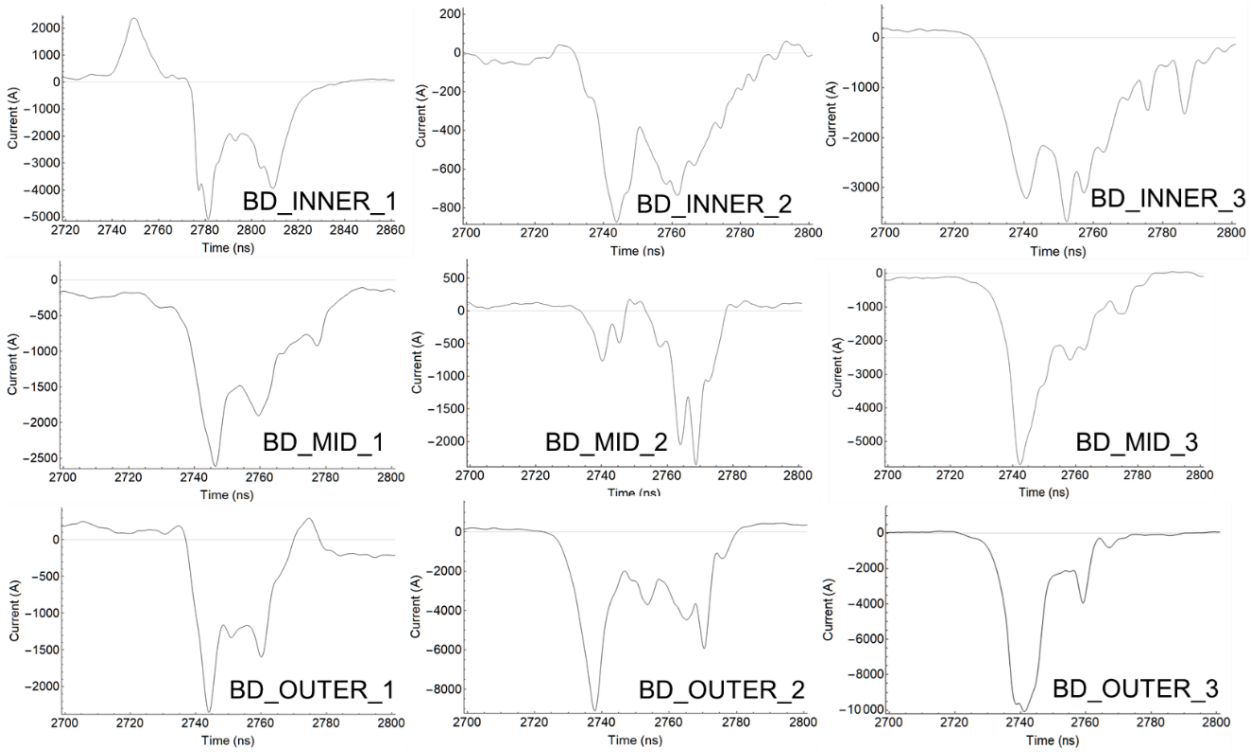

Figure 4-6. Processed current traces from shot 4460. Except for BD_INNER_1, all plots have the same time scale. The error in the signal magnitude based on the baselining technique alone is estimated to be around 500 V.

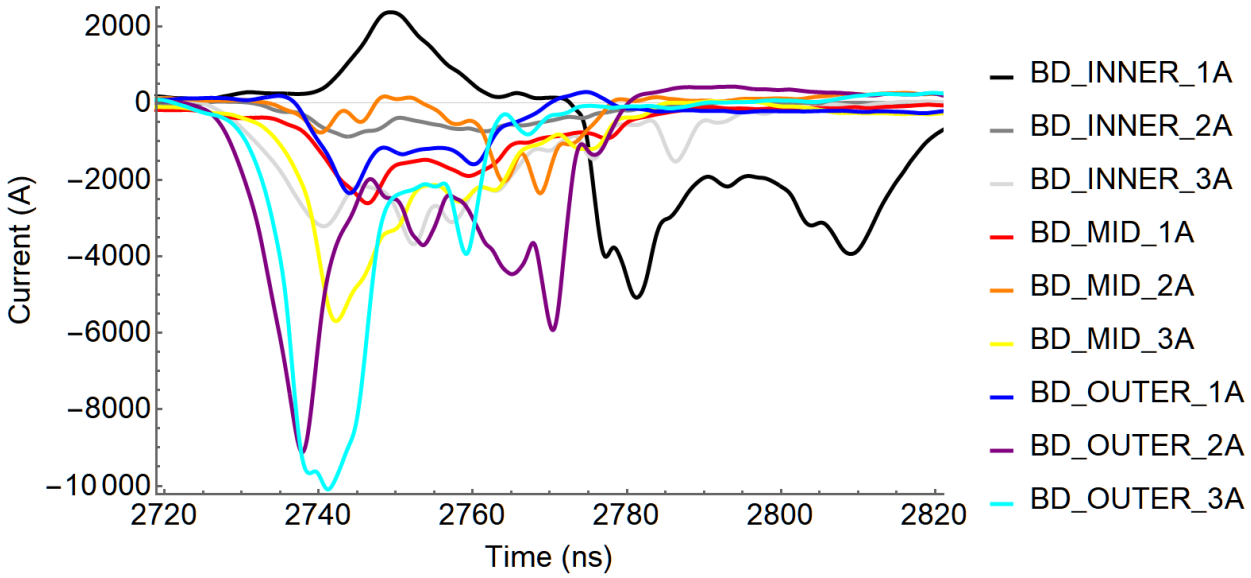

Figure 4-7. All pinhole currents for shot 4460.

4.1.1.5. Radiochromic films

The films on the top surface of the wedges, which was intended to provide a reference fluence, were shredded by debris and bullets as shown in Figure 4-8. Figure 4-9 shows the scanned films sandwiched inside the wedge. While all B3 films survived, only about half the V2 films were scannable. The V2 films appeared to be at a higher risk for delamination from its backer plastic film. The films show darkening only on a thin strip into the wedge. Recall that for ~1.5 MeV electrons we expect to see darkening approximately half-way up the film. These films show only low energy electron exposure again consistent with only low energy early time electrons before the load reaches full voltage.

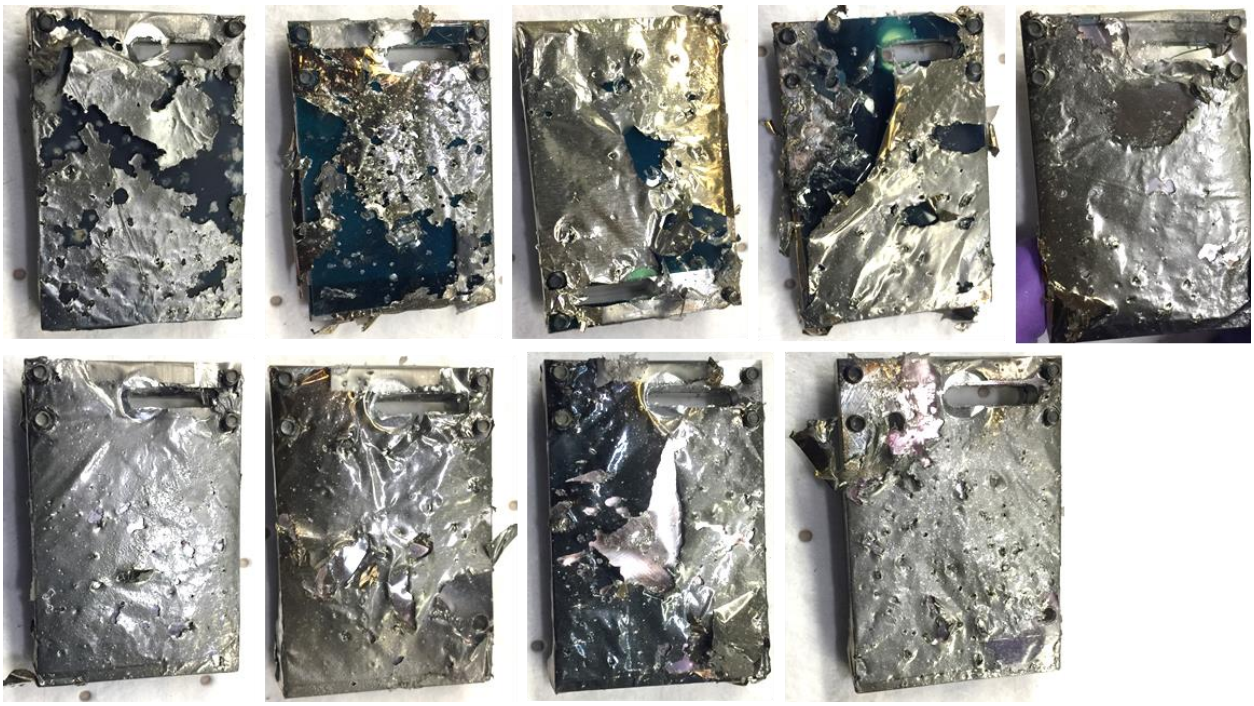

Figure 4-8. Photos of the top beam-facing surface of the wedges.

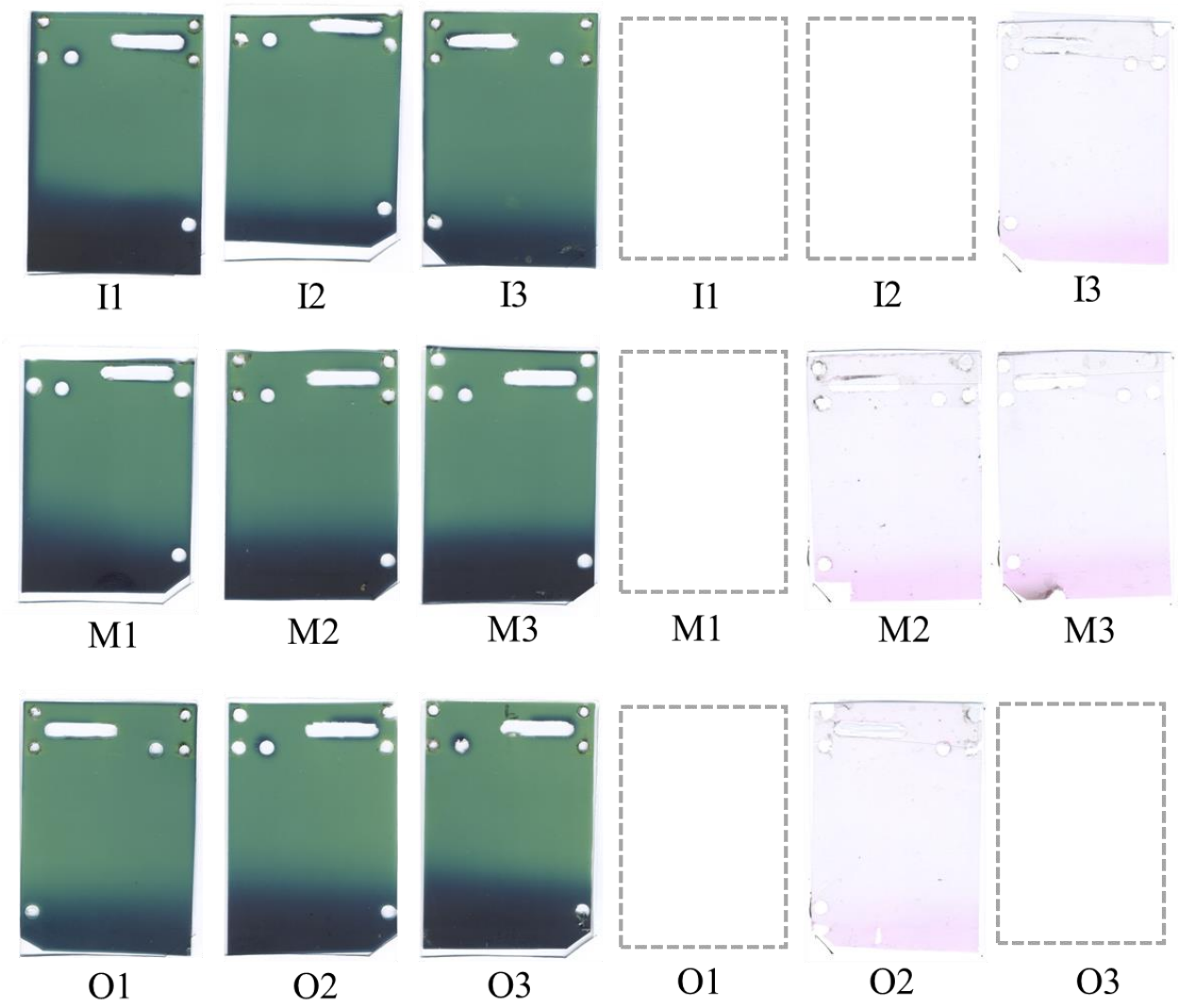

Figure 4-9. Scanned radiochromic films in between the wedges for shot 4460. I/M/O are the inner (upper) / middle / outer (lower) cathodes. The left (greenish) films are the V2 and the right (pinkish) films are the B3. Grey boxes represent films that were too damaged to scan.

4.1.2. Shot 4461 (Second shot)

The goal of the second shot was to find solutions to the debris problem and to get the electron beams to center up on the pinholes. We took two new actions in the setup, described below, to address these problems.

4.1.2.1. Setup

In order to mitigate the debris problem due to the spalled stainless steel beam-stop, we taped thick sheets of Kapton (Cirlex) around each wedge as shown in Figure 4-10. This material is often used for debris shields on Z experiments so we thought it was worth attempting here.

The wedges also had a different configuration. Instead of having separate B3 and V2 versions of the wedges, all wedges had both films on the top surface and the sandwiched inside the wedge. We also added an additional layer of Kapton film over the radiochromic films to provide resistance to debris. The wedges were again wrapped in aluminum foil as a final protective layer.

On the beam-stop, we changed out all pinholes to be the largest size, 6.10 mm diameter. The B-dots were cleaned up and reused. None of them appeared to have much damage other than some metal debris from the spalled beam-stop. We would have liked to replace the B-dots on every shot since there could be hidden damage in the connectors from shock, but reusing them was a practical decision since we did not have enough B-dots available that had good calibrations. Some of the SMA elbows were replaced due to visible damage. One of the SMA shorts on NOISE_1 was replaced with a B-dot mounted inside an aluminum can that had one end copper taped shut. This was intended to provide the B-dot cable drive noise in a field-free region. The attenuation was left at 20x.

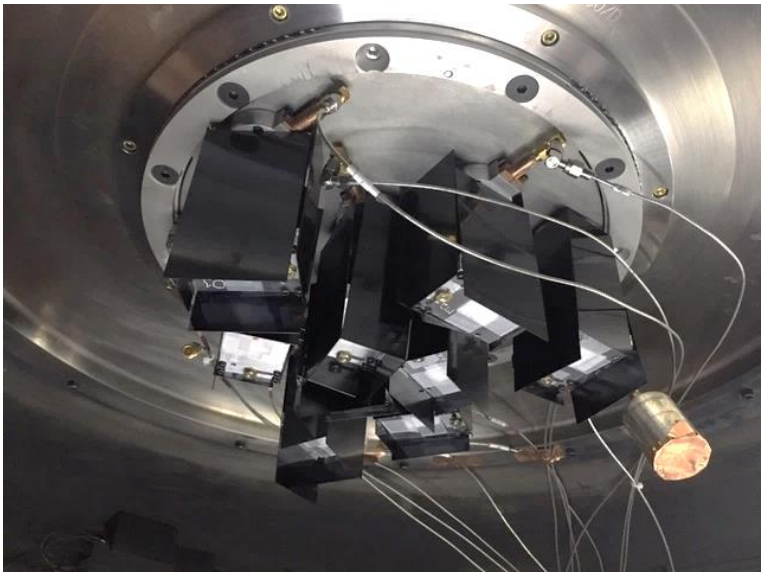

Figure 4-10. Photo of installed shot 4461 setup showing Kapton shields around wedges. The cylinder hanging in the lower right corner is a B-dot loop inside what should be a field-free region to get a cable noise measurement.

To deal with the problem of the electron beam not being centered on the pinholes, we chose to use the chamfered cathode tips for the middle and outer cathodes. The inner was not changed and remained as a standard flat tip. We were fortunate that there happened to be some chamfered tips available so no additional machining was necessary.

Table 4-2. Diagnostic setup for shot 4461

Signal Name	Detector	External Attenuation	Pinhole ø (mm)	Distance (mm)	Film Types
BD_INNER_1A BD_INNER_1B	B-dot 03	5x	6.10	88.7	B3/V2
BD_INNER_2A BD_INNER_2B	B-dot 06	5x	6.10	88.6	B3/V2
BD_INNER_3A BD_INNER_3B	B-dot 07	5x	6.10	88.3	B3/V2
BD_MID_1A BD_MID_1B	B-dot 09	5x	6.10	89.3	B3/V2

Signal Name	Detector	External Attenuation	Pinhole ø (mm)	Distance (mm)	Film Types
BD_MID_2A BD_MID_2B	B-dot 11	5x	6.10	88.8	B3/V2
BD_MID_3A BD_MID_3B	B-dot 12	5x	6.10	88.6	B3/V2
BD_OUTER_1A BD_OUTER_1B	B-dot 15	5x	6.10	88.3	B3/V2
BD_OUTER_2A BD_OUTER_2B	B-dot 16	5x	6.10	88.1	B3/V2
BD_OUTER_3A BD_OUTER_3B	B-dot 18	5x	6.10	88.2	B3/V2
NOISE_1	B-dot inside can	20x	N/A	N/A	N/A
NOISE_2	SMA short	20x	N/A	N/A	N/A

4.1.2.2. Machine performance

This was a 36 line shot with no significant issues noted by operations. The MTG spread was about 28 ns, slightly more than the target value. This was considered a good shot by all indications.

4.1.2.3. Hardware autopsy

Unsurprisingly, the Kapton shields were severely damage and found scattered over the vacuum dome. They were less effective though at shielding the debris from the wedges than we had hoped. This is likely due to the greatly enhanced debris on this shot compared to the previous due mainly to superior pulsed power performance resulting in a "hotter" shot. This is shown in Figure 4-11 with the enhanced spall pattern on the backside of the beam-stop. Even the pinholes experienced enhanced spalling. The Kapton sheets could not shield against spalling from the pinholes and this debris alone was enough to shred the upper surface films of the wedges.

Figure 4-12 shows the top surface of the beam-stop. The burn pattern is uniform and deep on all cathodes. It is also completely centered on the pinholes meaning our chamfered tips worked as intended. Comparing this burn pattern to that of the typical bremsstrahlung load shots, had this shot been a radiation producing shot, it is likely to have been a very high dose shot.

Figure 4-11. Bottom of the beam-stop for shot 4461 showing uniform spall pattern for all cathodes.

Figure 4-12. Top surface of the beam-stop on shot 4461 showing uniform burn pattern.

4.1.2.4. B-dot signals

The baselined and integrated B-dot signals are shown in Figure 4-13. While almost of the currents display two or more peaks indicating that the electron beam was sweeping dynamically across the pinhole, BD_INNER_1 shows the most prominent double peak structure. The peak current values for this shot were all significantly higher than the previous due to better alignment of the electron beams through the pinholes.

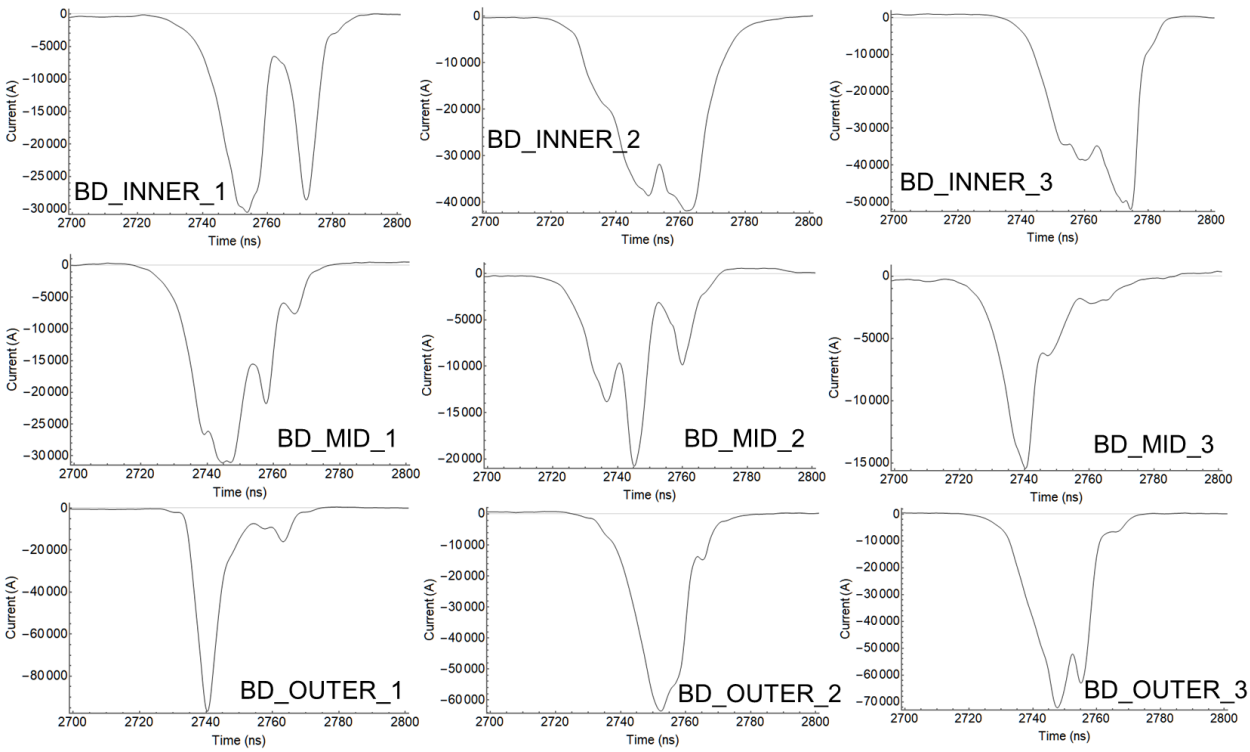

Figure 4-13. Processed current traces from shot 4461. All plots have the same time scale.

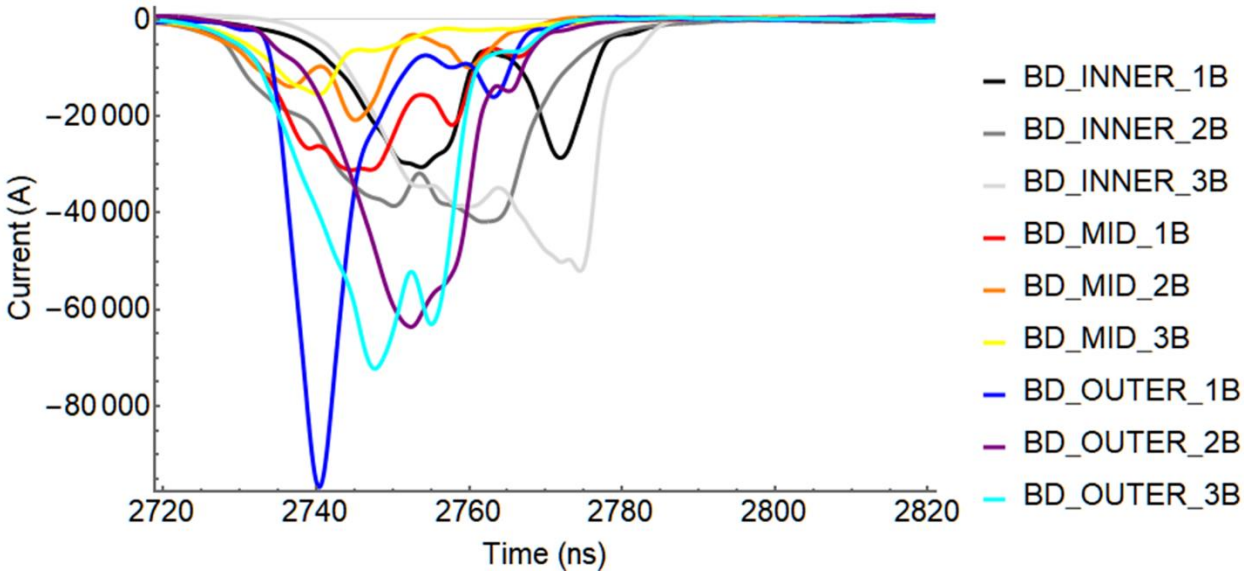

Figure 4-14. All pinhole currents plotted together for shot 4461.

4.1.2.5. Radiochromic films

Spalling again caused severe damage to the wedges. The top surface films were completely unusable as shown in Figure 4-15. Upon disassembly of the wedges we found that only the middle #3 and outer #1 films B3 were usable for analysis. The others had delaminated or been penetrated by bullets.

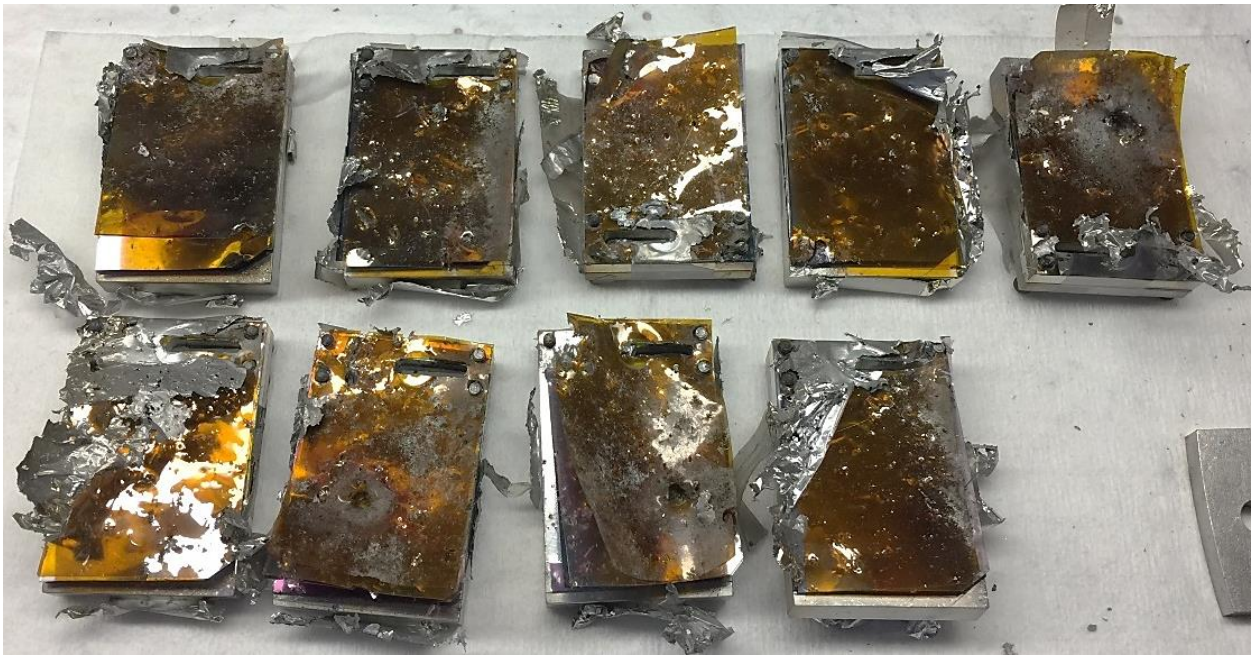

Figure 4-15. Remnants of wedges from shot 4461.

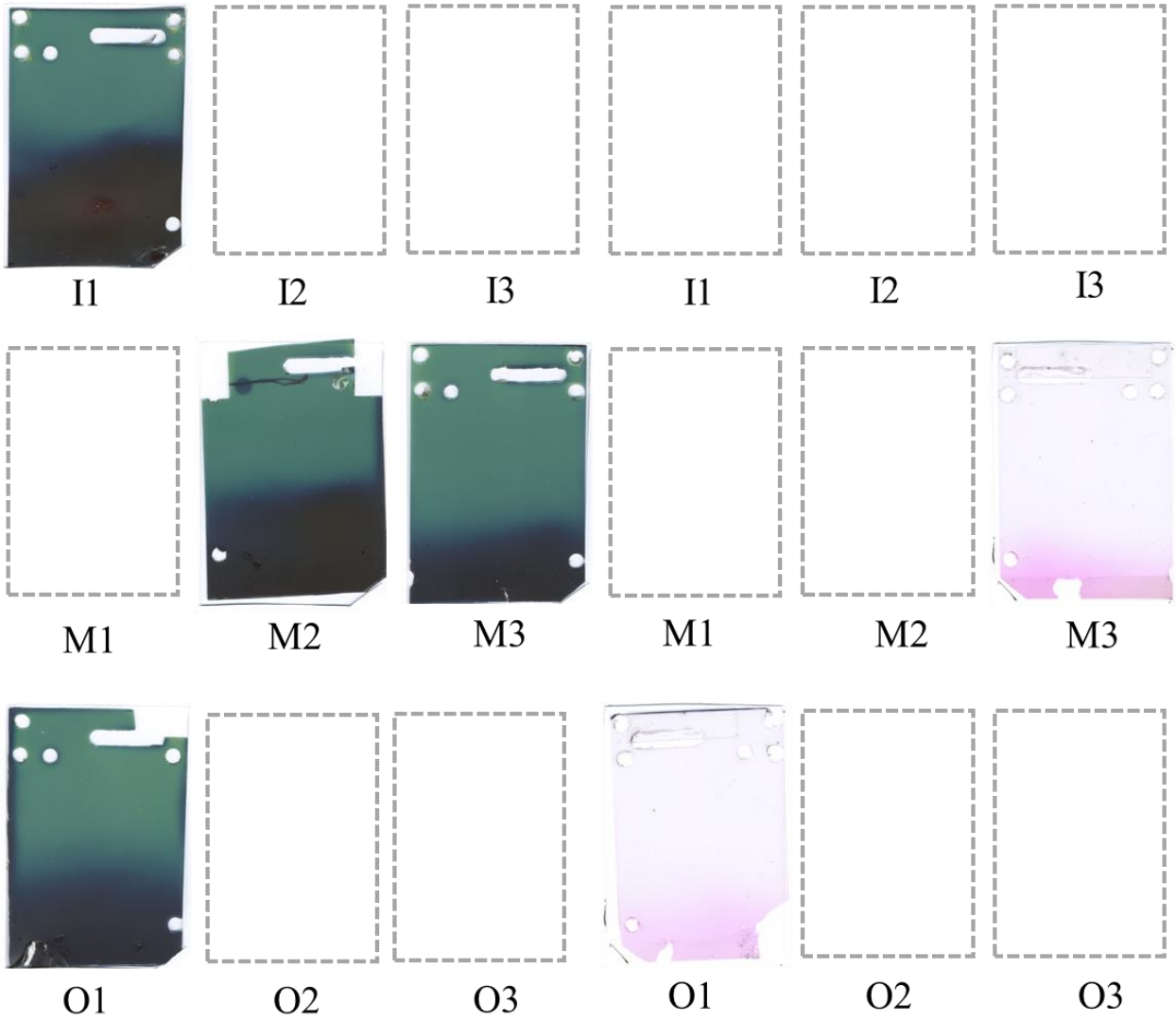

Figure 4-16. Scanned radiochromic films in between the wedges for shot 4461. I/M/O are the inner/middle/outer cathodes. The left (greenish) films are the V2 and the right (pinkish) films are the B3. Grey boxes represent films too damaged to scan.

4.1.3. Shot 4462 (Third and final shot)

Because of the continued spall damage to the wedges, it was decided to double up the beam stop using the hardware intended for the fourth shot. It was becoming increasingly unlikely that we would have enough time for a fourth shot so using the extra hardware to try to increase success of the final shot was the right choice.

4.1.3.1. Setup

The second beam stop was mounted on top of the first using two washers to provide some distance for the spalled metal to expand. The first beam stop did not have any pinholes mounted while the second had a few empty locations while the rest were the large 6.1 mm diameter pinhole. It was hoped that this additional spacing would also prevent the pinholes themselves from spalling so badly since the electron beams would have additional space to expand before reaching the pinholes. We

did not use the additional Kapton side shields. We again used the chamfered cathode tips since they worked well on the second shot in centering up the beam on the pinholes.

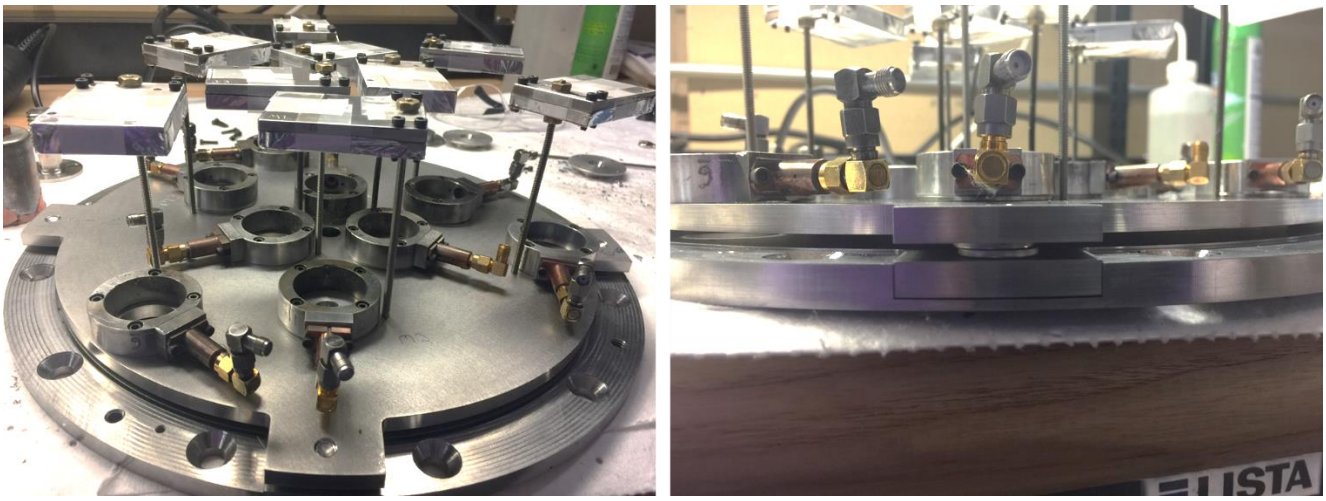

Figure 4-17. A second beam stop was mounted underneath the first to protect the wedges from spalled metal.

We chose to run several wedges without any pinholes in front to totally avoid spalling issues. To avoid saturating the radiochromic films, these wedges were positioned off axis of the beam-stop hole. M1 and O3 were completely off axis so they would only catch the edge of the expanding electron beam. I3 was positioned so the center of the electron beam would hit the edge of the wedge.

We again fielded the same noise channel diagnostics. For those B-dots without a pinhole, the attenuation was increased to 50x to compensate for the potentially much larger signal.

Table 4-3. Diagnostic setup for shot 4462

Signal Name	Detector	External Attenuation	Pinhole ø[1] (mm)	Distance[2] (mm)	Film Types
BD_INNER_1A BD_INNER_1B	B-dot 03	5x	6.10	89±2	B3/V2
BD_INNER_2A BD_INNER_2B	B-dot 06	5x	6.10	89±2	B3/V2
BD_INNER_3A BD_INNER_3B	B-dot 07	50x	none	89±2	B3/V2
BD_MID_1A BD_MID_1B	B-dot 09	50x	none	89±2	B3/V2
BD_MID_2A BD_MID_2B	B-dot 11	5x	6.10	89±2	B3/V2
BD_MID_3A BD_MID_3B	B-dot 12	5x	6.10	89±2	B3/V2
BD_OUTER_1A	B-dot 15	5x	6.10	89±2	B3/V2

Signal Name	Detector	External Attenuation	Pinhole ø[1] (mm)	Distance[2] (mm)	Film Types
BD_OUTER_1B					
BD_OUTER_2A BD_OUTER_2B	B-dot 16	50x	none	89±2	B3/V2
BD_OUTER_3A BD_OUTER_3B	B-dot 18	50x	none	89±2	B3/V2
NOISE_1	B-dot inside can	20x	N/A	N/A	N/A
NOISE_2	SMA short	20x	N/A	N/A	N/A

4.1.3.2. Machine performance

On first shot attempt, Marx 18 was bussed out due to a pre-trigger. It triggered early before the swing arms closed, also causing Marx 17 to prefire. On the second attempt, the Marx's only charged to 17 kV before pre-firing. Marx 17 was then bussed out. On the third attempt, the Marx's only charged to 10 kV before pre-firing. The shot was then delayed until the following Monday. The crew found a blown component on a walkthrough of the oil tank and Monday's shot was successful with all 36 lines.

The MTG spread for the shot was about 24 ns, slightly better than the target. Switch 19 ran slightly early. Overall, this was a decent shot.

4.1.3.3. Hardware autopsy

Spalling from the pinholes was again unavoidable and the top surface films of those wedges with pinholes were mostly destroyed as shown in Figure 4-18.

Figure 4-18. Photo of top surface of wedges showing damage from pinhole spall debris.

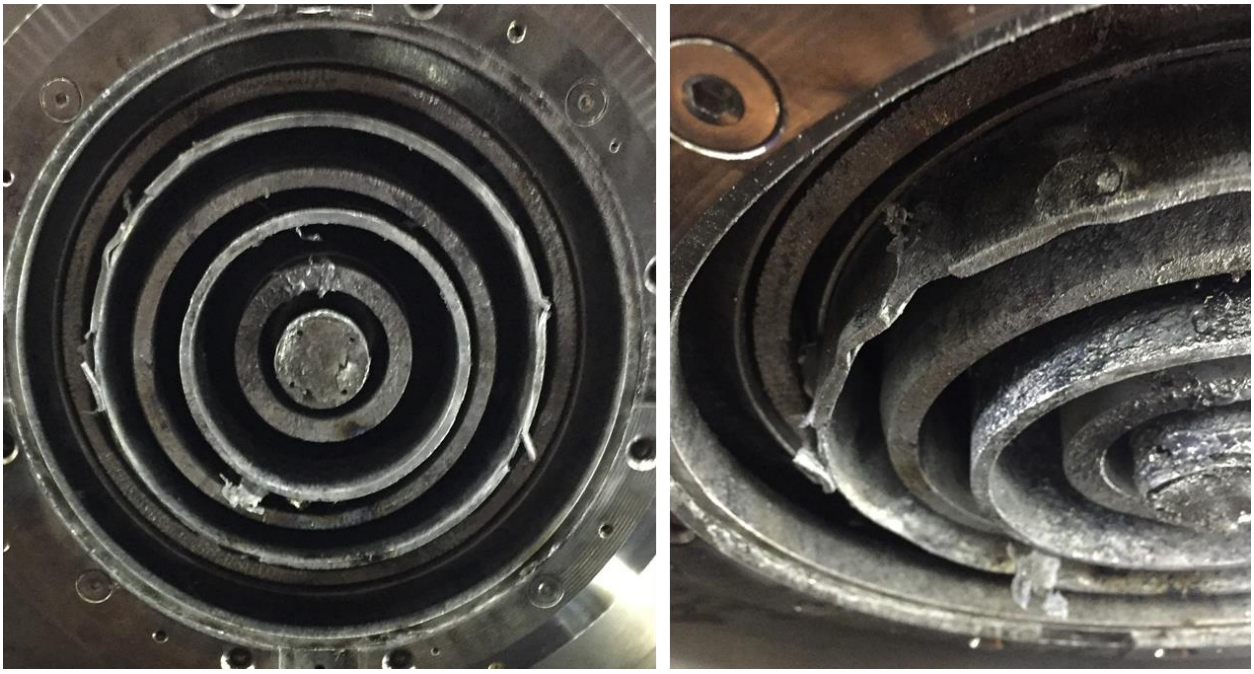

Figure 4-19. The remains of anode and cathode tips show that the electron beam struck the upper middle anode in several places causing spalling.

Figure 4-19 shows that the electron beam of the middle cathode walked radially outward on the anode foil and ended up depositing a significant amount of its energy into the upper middle anode tip, causing it to spall. This meant that there was only a very weak middle cathode burn as shown in the remains of the top surface of the upper beam-stop in Figure 4-20. The burn was likewise very

light on the inner cathode but that was due to the beam steering inward into the rocketship causing melting of the aluminum cup on the bottom of the rocketship.

The burn was very strong and uniform for the outer cathode. That means that the outer cathode was unaffected by any plasma created due to the beam interacting with the upper middle anode tip. This likely happened well after peak voltage.

One last feature worth mentioning is that the upper beam-stop still spalled as with the previous experiments. We purposed stood off the lower beam-stop to try to avoid transferred shock into the diagnostics attached to the lower beam-stop. Figure 4-21 shows that we didn't space them far enough apart. The spalled metal expanded into the gap between the beam-stops and became compressed. Certainly, there was still significant shock transferred to the lower beam-stop.

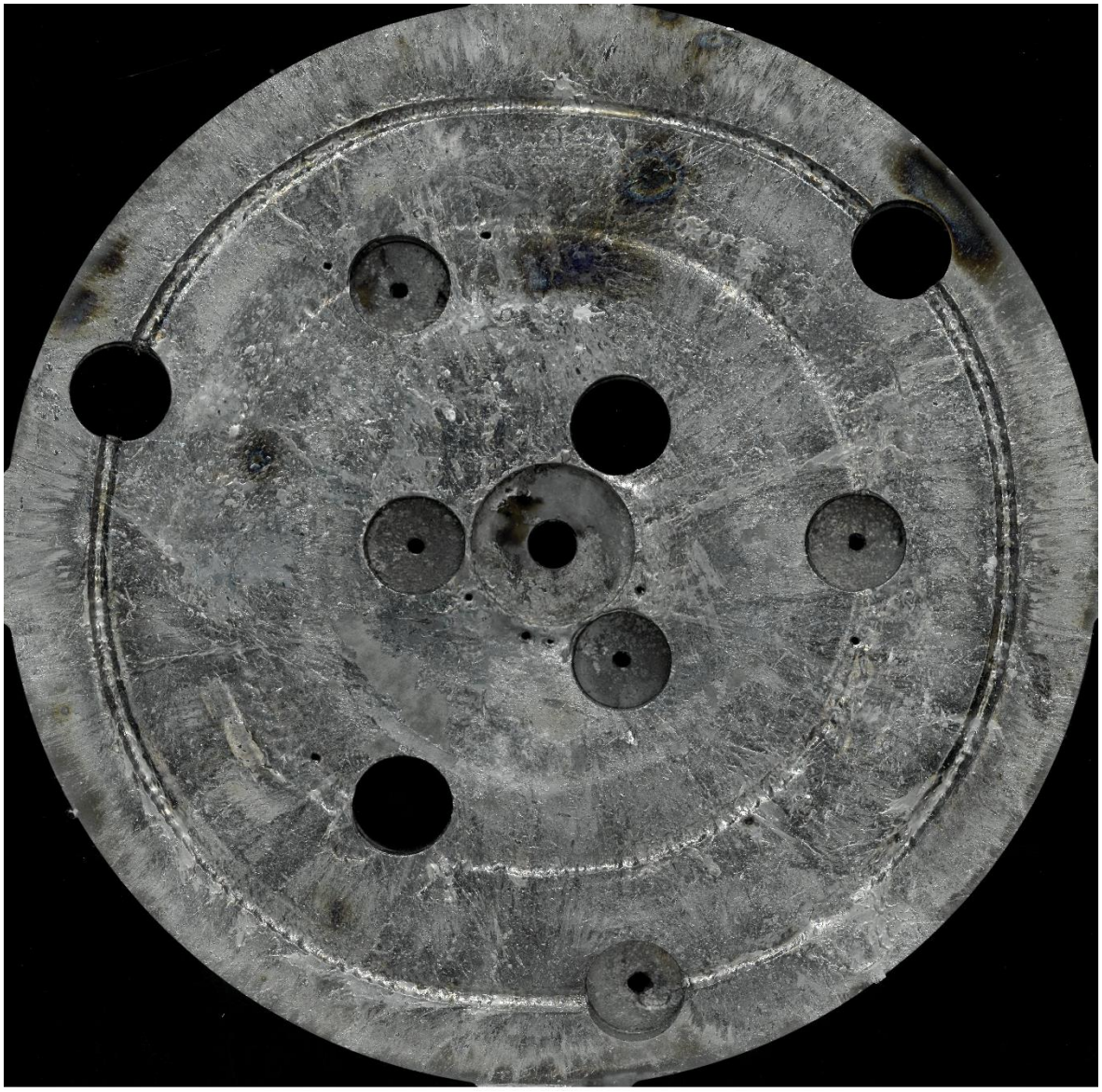

Figure 4-20. Top surface of the beam-stop from shot 4462.

Figure 4-21. The bottom side of the upper beam-stop showing spalled metal contacted the lower beam-stop.

4.1.3.4. B-dot signals

Several of the current signals for this shot showed problematic behavior. The currents are shown in Figure 4-22. The signals for BD_INNER_1 and BD_INNER_3 show reflections on the same time scale which suggests that perhaps the SMA connectors for both of these B-dots were damaged on the previous shot or there was a loose connection. BD_INNER_2 and BD_MID_3 is also appeared too large especially since they had pinholes. The signals for those channels lacking pinholes were not obviously larger.

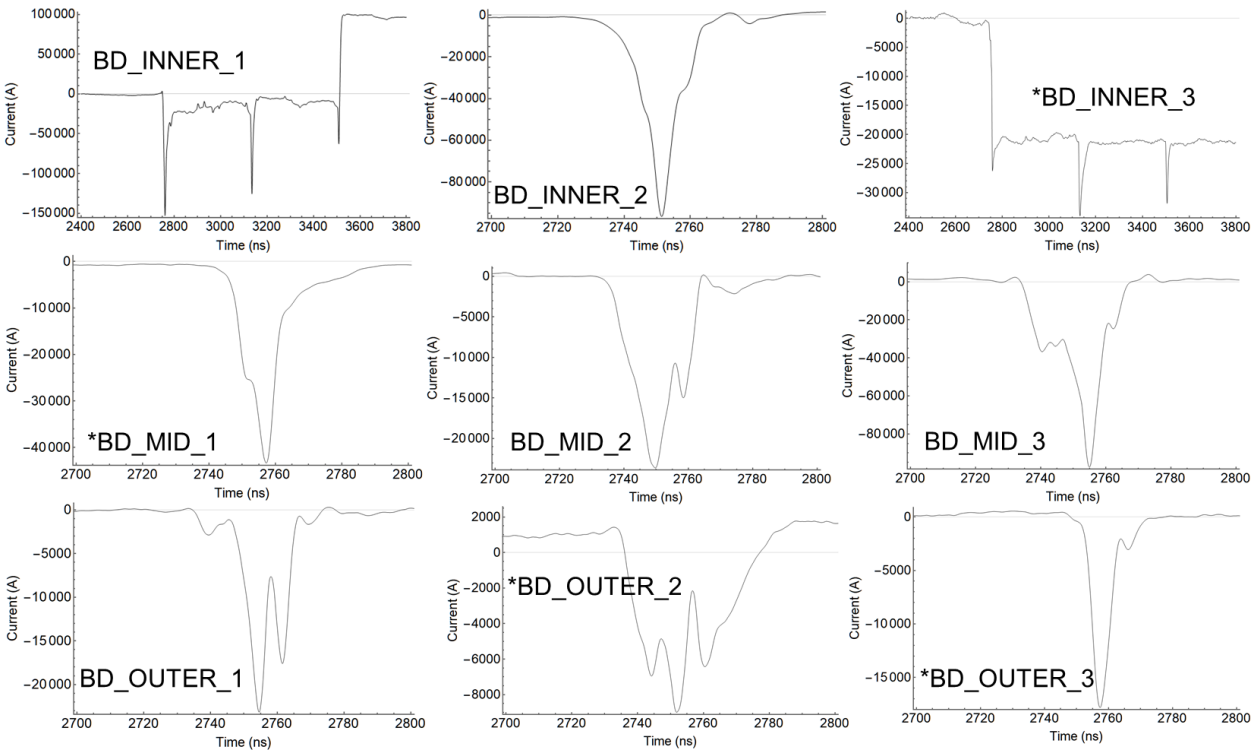

Figure 4-22. Processed current traces for shot 4462. Signals with an asterisk (*) are those that did not have a pinhole.

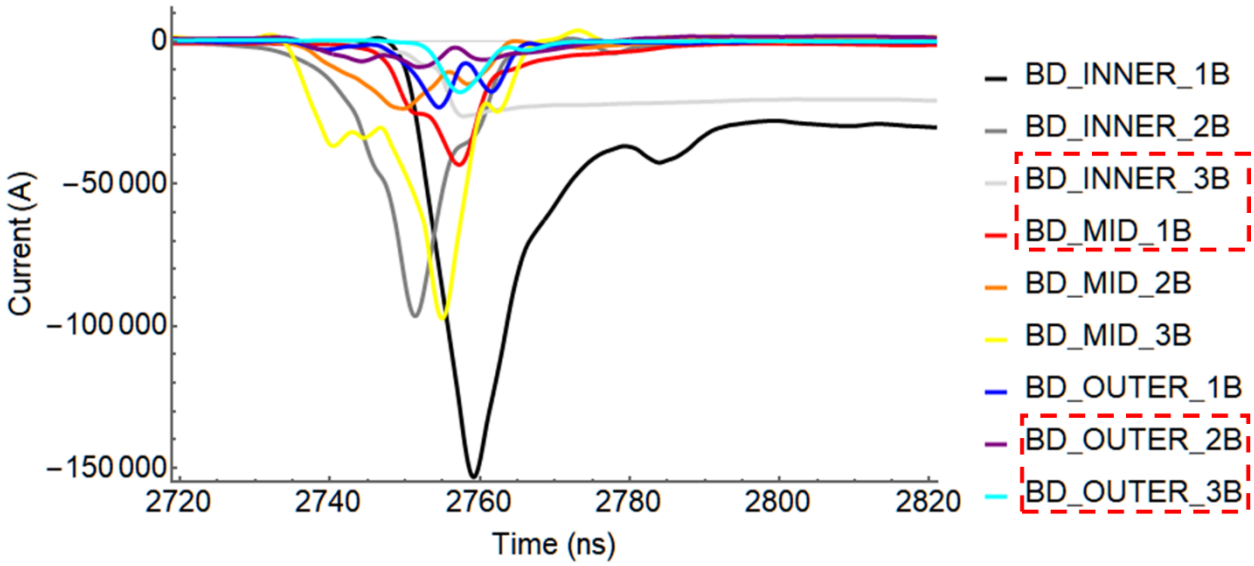

Figure 4-23. All processed pinhole currents. The signals inside the red dashed box had no pinhole installed. Signals BD_INNER_1 and BD_INNER_3 show signals reflections indicating a cable problem and so their magnitudes are suspect.

4.1.3.5. Radiochromic films

The films for this shot are significantly darker than both earlier shots. All films except M1 were scannable. With some pinholes missing, it appears that there was strong electron scattering in all directions causing electron penetration into the edges of the wedges, exposing the films around the

outer perimeter. The film is also exposed further along the wedge which suggests the electrons beams for all cathodes had higher energy than the previous shot.

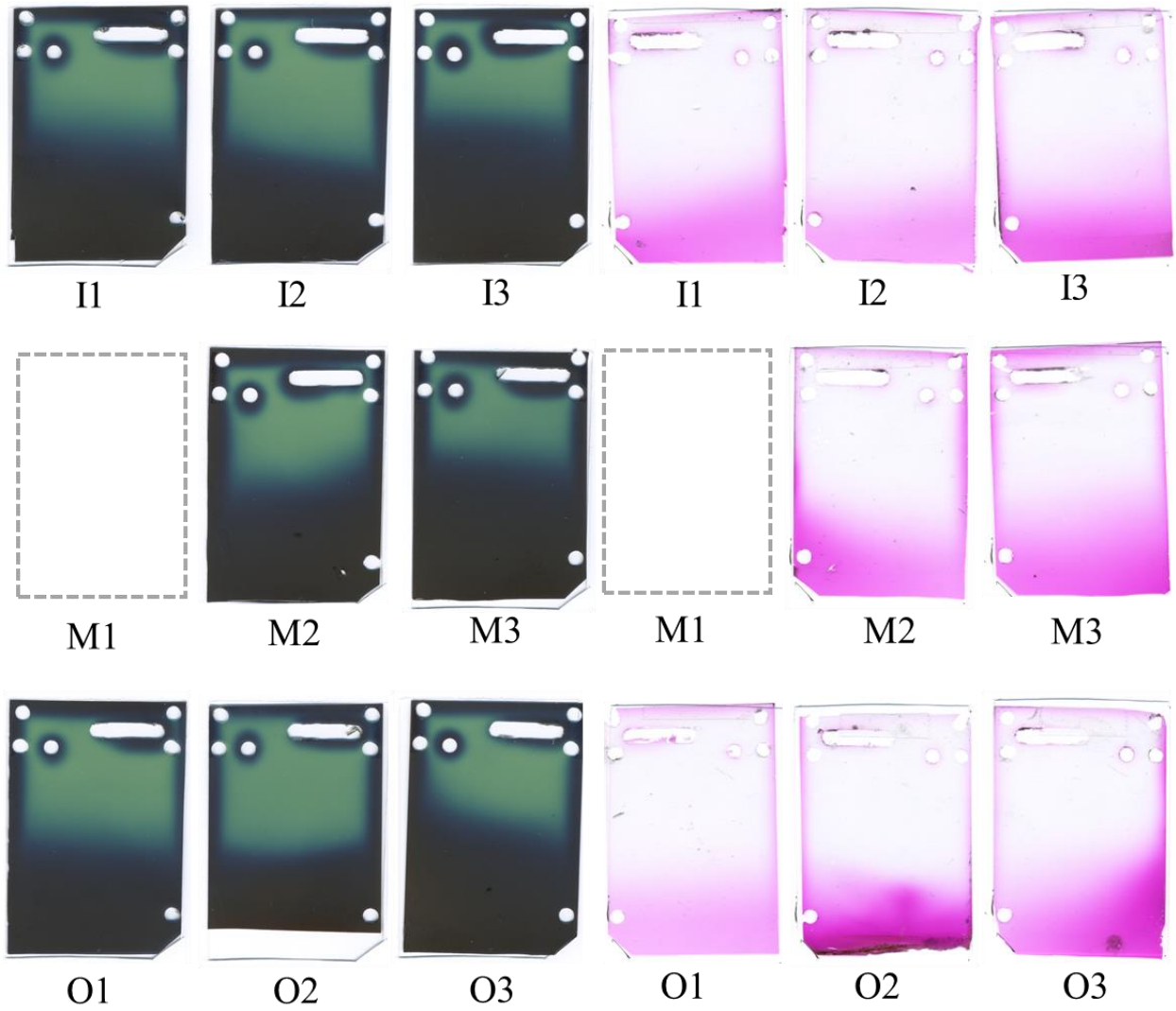

Figure 4-24. Scanned radiochromic films in between the wedges for shot 4462. I/M/O are the inner/middle/outer cathodes. The left (greenish) films are the V2 and the right (pinkish) films are the B3. Grey boxes represent films too damaged to scan.

5. ANALYSIS AND DISCUSSION

In this section, the results from the radiochromic films and currents are analyzed. The radiochromic films were interpreted using machine learning to convert scanned image data into dose measurements. The method used to train the machine learning algorithm is available in Appendix B. We attempted to use these analyses to compute an electron energy spectrum and compare to an MCNP simulation.

The current measurements from the B-dots are also given a closer look. The methods used to clean the B-dot data are available in Appendix A. The relative shapes of the pulses are compared across the three cathodes. The peak currents are compared to estimates made by some basic geometric considerations and are found for the most part to agree.

5.1. Interpreting the radiochromic films

To convert the image data of the scanned radiochromic film into a dose measurement and ultimately to an electron energy spectrum, there are several steps. This section describes how the image processing was performed on the scanned films and how we used a trained neural network dose predictor to create dose vs. distance profiles.

5.1.1. Scanning and image processing

Each film we chose to evaluate was image processed by cropping and rotating the image so that the wedge slope was in the +X direction. A series of 21 line-outs were taken in the area shown by the red box in Figure 5-1. This area was chosen because it avoided any edge bleed effects and the slot cut out.

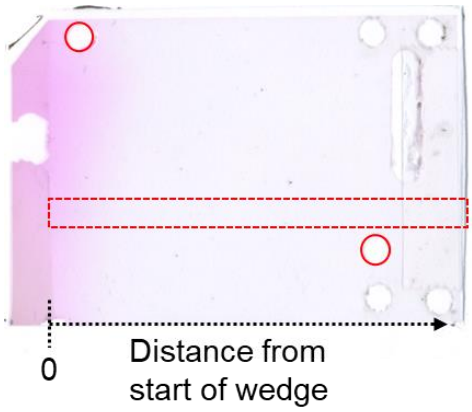

Figure 5-1. An example of a B3 film with a red outline of the region on each film that was analyzed. The red circles indicate the positions of the pins, used as a fiducial to determine the image scale of the scan.

5.1.2. Interpretation via machine learning

After the line-out data is run through the neural network dose predictor, we produce plots that look like Figure 5-2. The different colored dots represent different lineouts of the same film. The spread in dose before the noise floor is low which means that there is good uniformity across the wedge, perpendicular to the wedge direction. This means the incident beam was uniformly filling the wedge as we desired and as we assumed for our MCNP response function simulations.

The plots always show a noise floor that occurs slightly below 1000 Gy where the dose rapidly drops. We are calling the corresponding distance, the cut-off distance, which will become important in predicting the end point energy of the electron energy spectrum. There are two possible explanations for the existence of this sharp drop. First, the lowest dose calibration swatch was 1000 Gy so it is possible that neural network algorithm lost fidelity below this level and went to noise. The 1 Gy floor is artificial. The 0 Gy dose calibration was changed to 1 Gy to prevent instability in the algorithm.

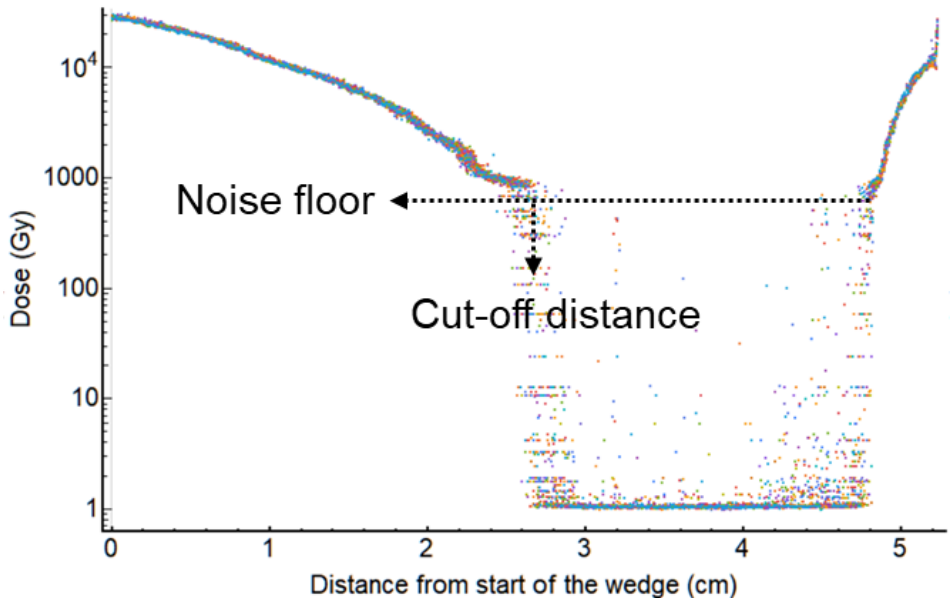

Figure 5-2. An example output of the neural network predictor, dose vs. distance along the wedge.

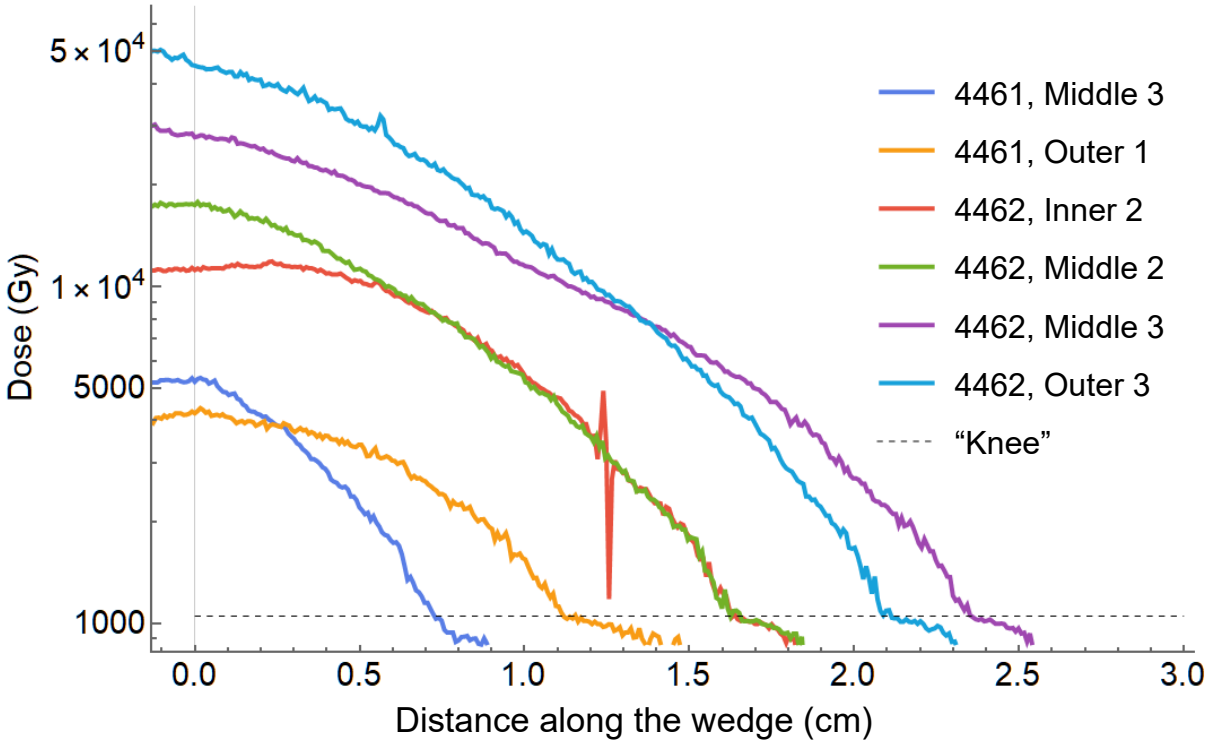

Figure 5-3. The median value of dose vs distance along the wedge for the six analyzed films. The noise spike in the red curve was the result of a piece of debris embedded in the film.

Six films were the focus of the analysis, two on the second shot and four on the third shot. Because the beams missed the pinholes on the first shot, the electron deposition into the wedges was small and therefore the doses in the films were too low to analyze. The plots shown in Figure 5-3 are the median value of the 21 lineouts for each film. The dose deposited on the second shot, the blue and yellow curves, was quite a bit lower than on the third shot. It is difficult to determine why this was the case since the beam-stop-as-witness-plate showed that the second shot was quite a bit better than the third, as far as the beams going straight into the pinholes. It is possible that the absence of some pinholes on shot 4462 caused a large number of electrons to scatter off the entire diagnostic plate caused greatly enhanced dose deposition coming from in all directions. That matches the evidence of the large amount of dose "bleed" from the edges of the wedges. If that is true, then it may be difficult to separate the electron dose from the enhanced bremsstrahlung dose from all those scattered electrons, since the low energy scattered electrons may have a similar linear attenuation distance as the electrons.

5.2. End-point energy of electron spectrum

Typically, the depth-dose profile technique is used to make a simple estimate of the end-point energy of the electron beam. The easy way to do this is to look at the cut-off distance along the wedge and compare that to the simulated dose-distance response functions. Figure 5-4 shows the same dose-distance curves from Figure 5-3 but normalized to the start of the wedge. Plotting this way, it is more obvious that the dose-distance curves each have two unique features that we have called the "knee" and the cut-off. The knee is the abrupt change in the slope that as shown in Figure 5-3, happens to occur around 1000 Gy. This feature could be due to either the bremsstrahlung background overtaking the dose contribution of the electrons, or it could be an artifact of the neural

network since as mentioned earlier, 1000 Gy was the smallest calibration dose. The "cut-off" is the feature where the dose rapidly drops to zero. This is the distance along the wedge where the neural network dose predictor shows effectively zero dose deposited.

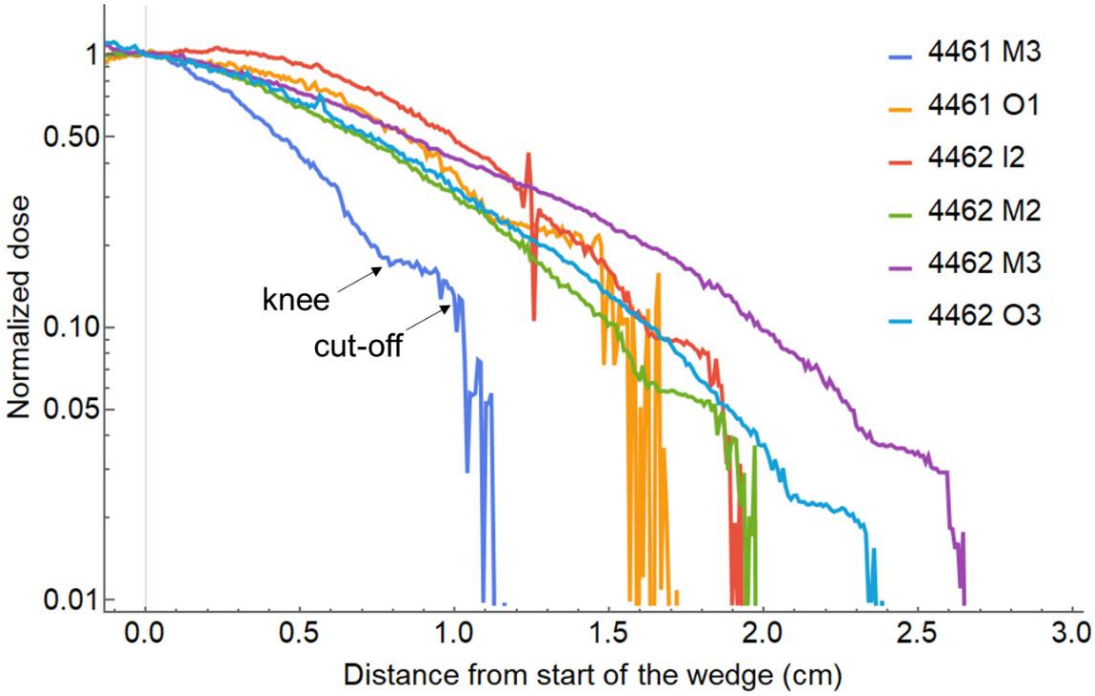

Figure 5-4. Dose-distance curves normalized at the start of the wedge used to compare the cut-off distances. The position of the "knee" and "cut-off" are shown for one of the wedges, which is used to estimate the electron end-point energy range.

By placing two points on the normalized monoenergetic dose-distance simulated functions for each wedge matching the position of the knee and the cut-off, we can draw a line between them as shown in Figure 5-5 . The simulated monoenergetic curves that are crossed by this (dashed) line gives a range of the approximate cut-off energy. The results are summarized in Table 4. The end-point energies are lower than expected for shot 4461 while for shot 4462, more in line with the expected end-point energy range typically quoted on Saturn as between 1.5 and 1.8 MeV.

Table 4. Estimated end-point energy ranges for the wedges by simple comparison to simulated monoenergetic dose-distance curves.

Wedge	End-point energy range (MeV)
4461 M3	0.87 – 1.02
4461 O1	1.2 – 1.43
4462 I2	1.43 – 1.51
4462 M2	1.35 – 1.47
4462 M3	1.75 – 1.9
4462 O3	1.55 – 1.67

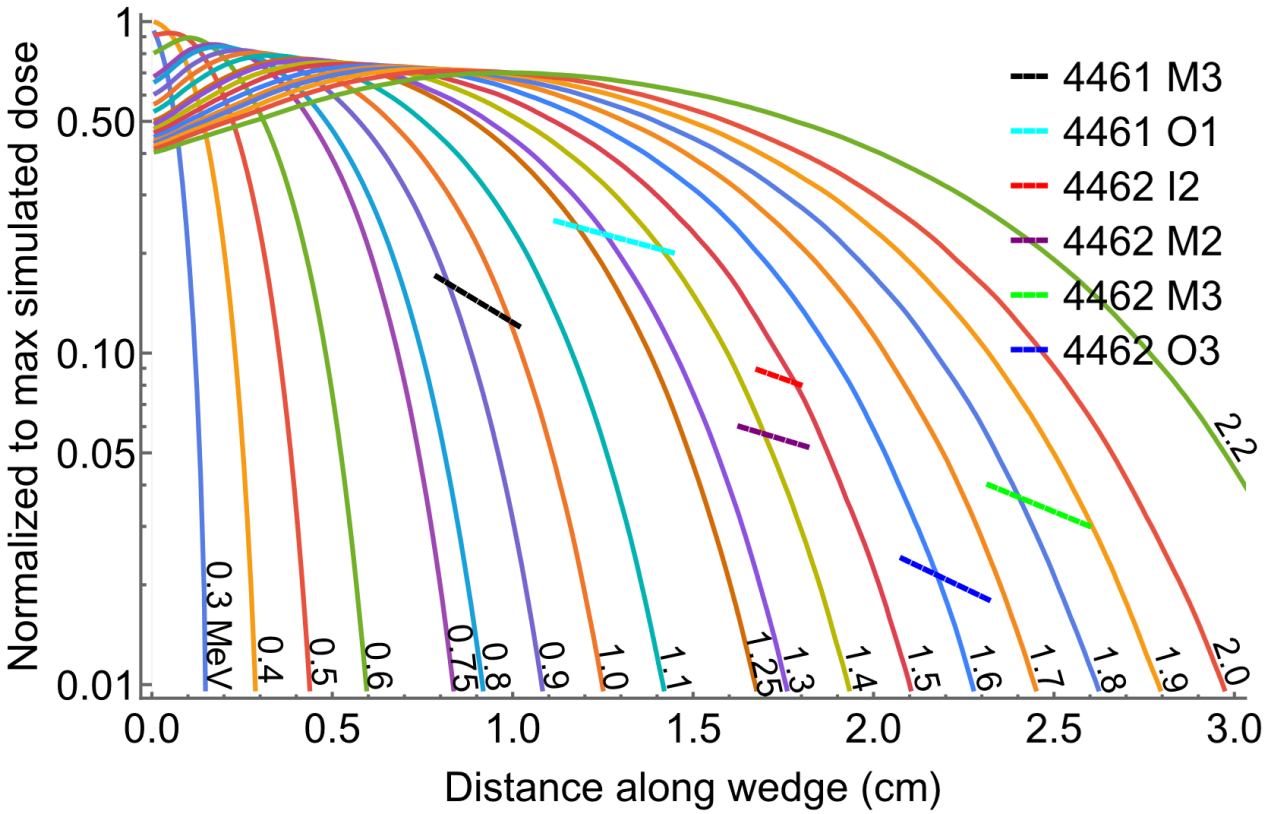

Figure 5-5. The end-point energy range is where the dashed lines cross the solid lines of the simulated mono-energetic dose-distance response functions.

5.3. Unfolding an electron energy spectrum

The formula for dose as a function of distance along the wedge is:

$$D(z) = \int_0^{E_{max}} f(E)d(z,E)dE$$

where f(E) is the electron energy spectrum and d(z,E) are the dose-distance response functions. Ideally one could construct an optimization routine using this formula to determine the energy spectrum that best matches the measured dose data. This analysis was performed without an optimization routine by manually tweaking the fractional contribution of each response function, attempting to match the dose data by iteration.

The fits to the data are shown in Figure 5-6. The test spectra and the data are both normalized to 1 at the start of the wedge. The fit iteration progressed by concentrating on the higher energy bins first to fit at large distances along the wedge, then focusing on the shape of the fit at smaller distances by increasing the contribution of the lower energy response functions. A general smoothness criterion was imposed used meaning that sharp changes were to be avoided, except at the high energy cut-off. Using this method it is possible to fit the entire range of dose deposition along the wedge, even going so far as to account for varying behavior on the shallow distance end such as the difference between 4461 Middle 3, where the dose deposition starts to decrease immediately inside the wedge compared to 4462 Inner 2, where the data do not peak until around 0.4 cm inside the wedge.

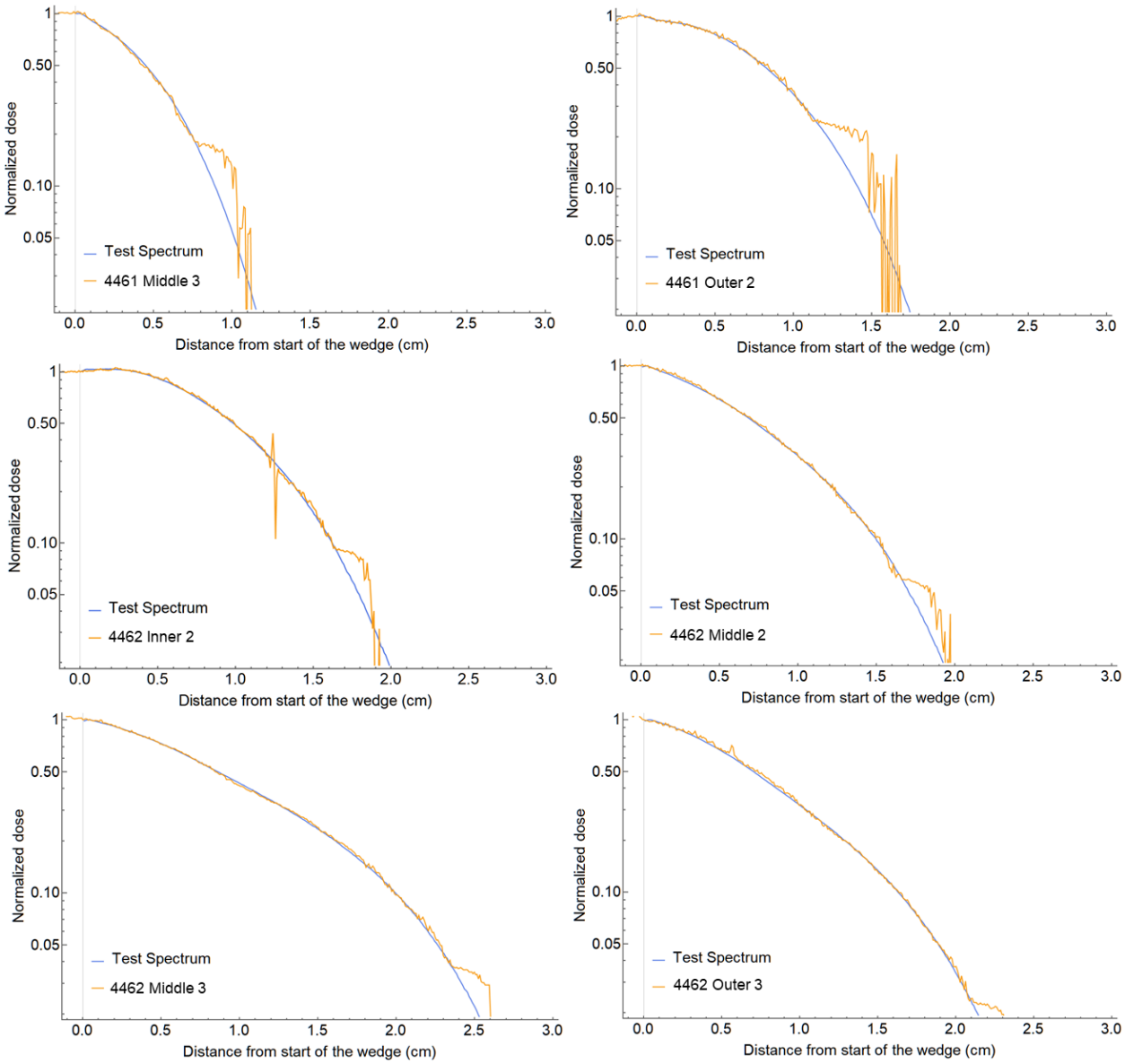

Figure 5-6. Normalized dose verses distance along the wedge compared to the test spectrum. It is possibly to produce excellent fits to the data by manual iteration all the way to the knee.

The spectra that produced these fits are shown in Figure 5-7. The trend for all spectra shows significant fraction of low energy electrons that decrease with increasing energy before hitting a peak and abruptly cutting off to zero. The fits were found to be most sensitive to the higher energy content. The low energy content came into play primarily through the renormalization of the spectra and trying to exactly match the initial dose fall-off inside the wedge. For shot 4461, the spectral peaks have energies of 1.0 MeV and 1.3 MeV. That is a little low compared to the typical stated end-point energy of Saturn based on circuit simulations and x-ray energy unfolds of 1.5 to 1.8 MeV. For shot 4462, the peak energies are higher with one of them, Middle 3 showing a peak of nearly 2.0 MeV with some fraction >2.0 MeV. It is difficult to say with certainty how real that is for the reasons stated in the previous section, however the fits to shot 4462 were just as good as for 4461.

Some time was spent to get a feel for the uniqueness of the solutions and it was found that it wasn't possible to find additional solutions with vastly different shapes that matches well at all wedge distances of the dose-distance function. This gives us confidence that at the very least, the shapes are correct. The contribution of each energy response function could be wiggled by a few percent without making the fits drastically worse.

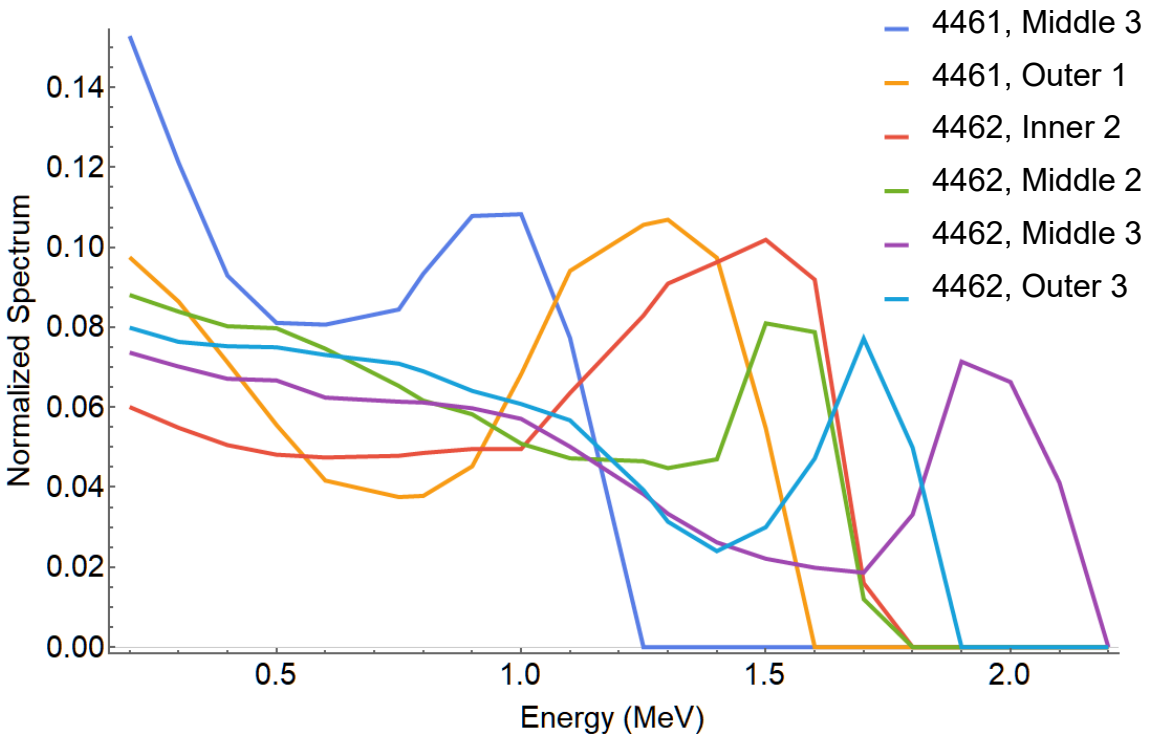

Figure 5-7. Unfolded electron energy spectra.

5.4. Comparison to an MCNP simulation

We wanted to compare our results to a simulation of the spectrum so we again used MCNP6 to run a test electron beam through our scattering foil and tally the electron spectrum as in Figure 5-8. The

voltage of the beam was modeled using calibrated V-dot measurements in the A-level vacuum flare from shot 4529, which were then used by Mark Savage to calculate a load voltage.

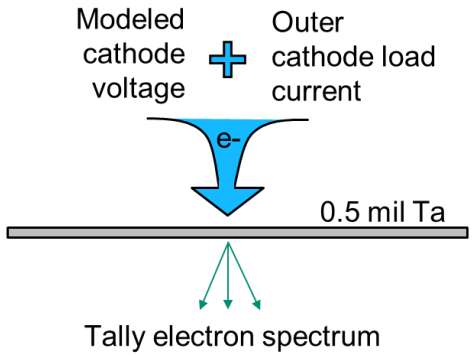

Figure 5-8. Diagram of the MCNP simulation of the electron energy spectrum from a Saturn outer cathode.

The window for when to start and end the pulse was done by via a multi-step process. First, a common timebase between shot 4529 and shot 4462 was found by computing an average A level current from the MITL B-dots and determining a relative timeshift for the 4461 and 4462 signals where the rise of the current pulses is reasonably aligned. This happened to be 20 nanoseconds for shot 4461 and 18 nanoseconds for shot 4462. Then the wedge currents were timeshifted by those amounts so that they could be plotted on top of the shot 4429 load voltage calculation as shown in Figure 5-9. The current used for this MNCP simulation was taken from an upstream averaged B-dot measurement on shot 4429 in the A-level transmission line which was then timeshifted to the load. The same cut-off window was applied.

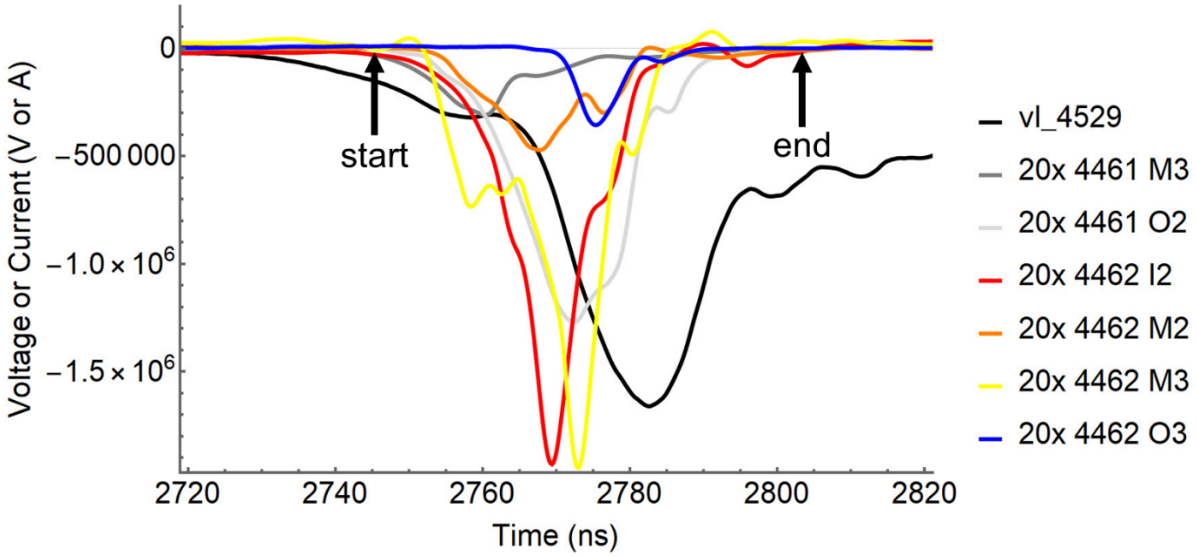

Figure 5-9. The load voltage (vl_4529) used in the simulation with the start and end times provided by comparison to the time-aligned wedge currents (scaled by 20x to better show the foot and tail of the signal).

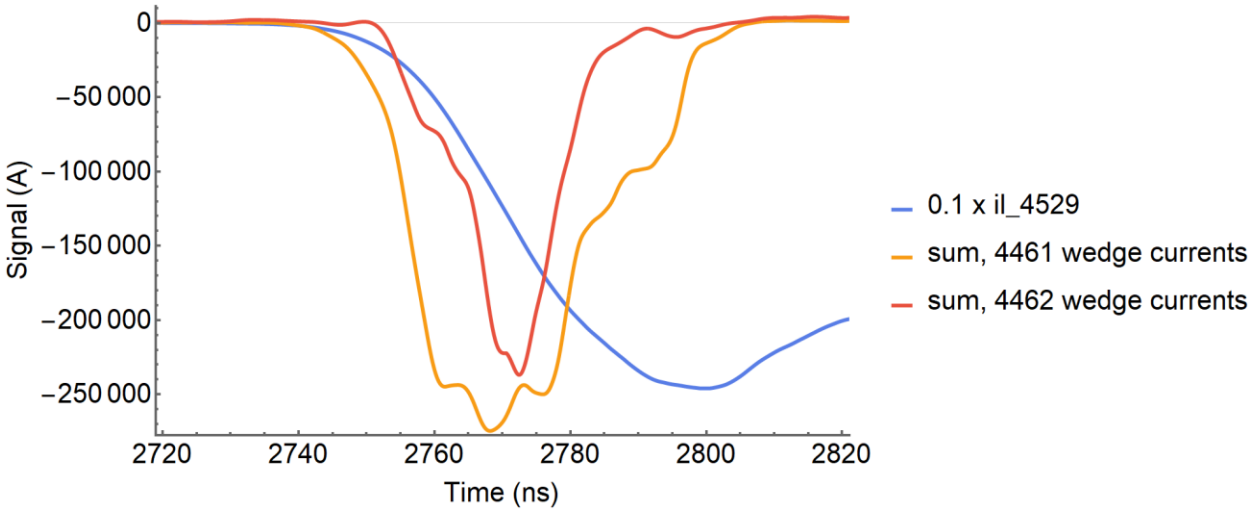

Figure 5-10. The current used (scaled by 0.1, shown in blue) for the MNCP simulation compared to the time-aligned sum of the wedge currents for the two analyzed shots.

The simulation shows that the thin 0.5 mil tantalum behaves as we expected, scattering the incident electron energy spectrum but not changing the general shape of the incident spectrum by much. Using the current and voltage values from the shot 4429 measurements and calculations, the MNCP simulation predicts a low number of low and medium energy electrons relative to our spectral fits. They peak around 1.6 MeV before abruptly cutting off, which is where the load voltage peaked. There is also a huge peak around 0.6 MeV, that we did not see in our spectra, due to the input voltage have a very slow decay from around 0.6 MV. Likewise, this simulation doesn't predict such a large fraction of electrons below 0.5 MeV that show up in our spectral fits. This is likely due to electrons that have scattered one or more times off the various surface around the pinhole and B-dot monitor ring before finding their way into the wedge.

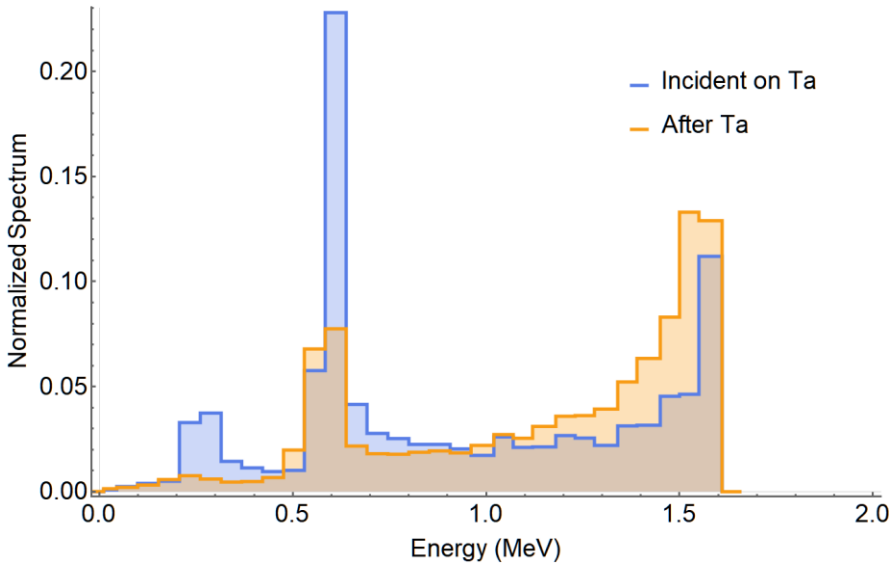

Figure 5-11. Results of the simulation showing the incident and transmitted electron energy spectrum through the Ta anode foil.

5.5. A closer look at the current data

The most important assumption we are making when analyzing the B-dot currents is that no matter how the baseline corrections are performed, the integrated signals must return to zero. It was assumed that the electron beam pinch may not pass directly through the pinhole, rather it is more likely to sweep across the pinhole and so we may see multiple peaks and/or a complex shape of the current pulse. However, the position of the B-dots, and the thickness of the beamstop meant that at some point in time, there would be no more beam coming through the pinhole and the B-dot would not register a signal. Figure 5-12 shows that the time envelope of the signals for shot 4461 is about 60-70 ns, for shot 4461 it is about 60 ns, and for shot 4462 it is 50 ns. The data for shot 4461 are most reliable since it was both a good shot and all monitors seemed to work properly.

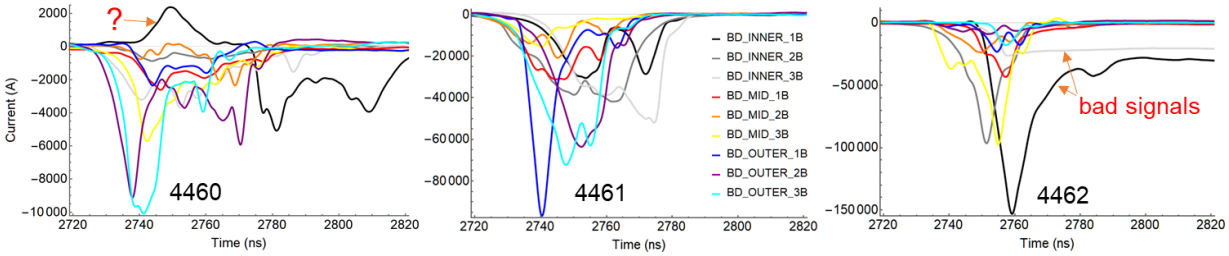

Figure 5-12. The pinhole currents for all shots showing the envelope of the signals in time.

We can calculate reasonable predictions to compare to these results for the inner and outer cathode peak currents by making some assumptions. First, for the inner current the circumference of the middle of the tip is 22.0 cm. The F-level median peak current has been calculated as 0.96 MA, so a simple estimate (assuming a doubling of the F level current) of the inner cathode peak current is approximately 1.9 MA. That gives us a linear current density of ~86 kA/cm. The A-level median peak current has been calculated as 2.29 MA, so a simple estimate (assuming a doubling of the A level current) of the outer cathode peak current is approximately 4.58 MA. That gives us a lower linear current density of ~63 kA/cm on the outer cathode. We can make an estimate of the number of pinches per length on the cathode through a visual analysis of hardware from a Saturn shot in January 2021 that saw significant beam steering from the middle cathode into the lower middle anode tip. This caused regularly spaced pitting from the pinched beams as shown in Figure 5-13. The average inter-pit distance was measured as 0.277" ≈ 0.7 cm. This implies ~3.6 pinches/in or 1.4 pinches/cm hitting the lower middle anode tip. The density would be higher coming off the middle cathode due to radial spreading, by a factor of the ratios of the two circumferences, 1.15, so there are 4.1 pinches/in or 1.6 pinches/cm on the middle cathode. If we assume that the inner and outer cathode have the same number of pinches per cm, then the inner cathode would have about 54 kA/pinch and the outer cathode is about 40 kA/pinch.

Figure 5-13. A photograph of the lower middle anode tip after a shot with significant beam steering off the middle cathode. The regularly spaced damage is a result of pinched beam strikes and was used to estimate the number of pinches per circumferential length of the cathode.

The large pinhole is 0.61 cm so it we should expect to see approximately one pinch of ~54 kA on the inner cathode. When comparing the data for shot 4461, the inner cathode currents showed peak values of 40 to 50 kA, matching the estimate. For the no-pinhole case on shot 4462 for INNER_3, the opening is about 3.2 cm so the current could be as high as double, up to 112 kA. For shot 4462, the open pinhole showed ~150 kA peak, much higher than the estimate but the signal quality was poor. For the outer cathode current, we should again see pinch current of about 40 kA. Shot 4461, with its generally more reliable data, shows peak currents above this estimate, in the range of 60 kA. For the no pinhole case as in shot 4462 OUTER_2 and OUTER_3, we could expect currents of about 80 kA. We did not see such large currents on these monitors; they were less than 30 kA.

6. CONCLUSION

We have demonstrated a new technique for directly measuring the electron energy spectrum in the Saturn 3-ring bremsstrahlung diode. We fielded a modified version of the diode to extract an electron beam passing through the thin scattering foil, through a pinhole inset in a total stopping stainless steel beamstop and into a depth-dose wedge. We adapted the depth-dose wedge technique used successfully on the RITS-6 accelerator by modifying the geometry of the wedge for a much shallower angle due to the smaller penetration depth from lower energy electrons. We found the electron beam expanded uniformly across the wedge, which was a primary initial uncertainty. We measured the beam current extracted through each pinhole using a Z-load style B-dot loop monitor.

In the experiment, which took place over one week, we took three shots and focused our analysis on the last two. The films were scanned and six of them were chosen to be thoroughly analyzed using a neural network machine learning algorithm to extract their dose-distance profiles. We simulated a set of dose-distance response functions of monoenergetic electron beams incident on our wedge using MCNP6 and used these functions to determine an electron beam end-point energy and to then unfold the electron energy spectra of these films.

In our findings, we were able to find that the end-point energy of the electron beams reasonably matched previously measured end-point energies of the x-ray radiation environment of the 3-ring bremsstrahlung source measured using differential absorption spectroscopy. Although this experimental analysis was no more precise then the x-ray techniques, it confirmed that the depth-dose wedge technique is valid for lower energy electron beams and therefore could be further refined. We also determined through the current measurements that the beam current extracted through the pinholes roughly matched predictions made using other techniques.

6.1. Suggested revisions for a follow-on experiment

In this final section of the report, we would like to capture some ideas for improvement should this experiment be performed again in the future. To achieve success, the focus needs to be on minimizing the debris generated from the beamstop and pinholes. To that end, the beamstop should be made thicker than 0.250", perhaps 5/16" or 0.312". Additional thicker beamstops should be prepared and used if spalling is still evident. The pinholes themselves should be made from tungsten. This will greatly increase their cost and increase the bremsstrahlung background but should they survive as intended they would be reusable and the top film uniformity and incident dose fiducial would be useful in the analysis.

To more successfully measure the beam currents, we suggest multiple Z load B-dots per pinhole so they could be averaged or use of Rogowski coils. Extra care needs to be taken in the routing of the cables as the number of connectors on the beamstop will make the layout difficult. It is recommended to have small jumpers pre-attached to the B-dots and tightened on the benchtop before mounting the beamstop. Some sort of metal shielding should be in place between the electron beam transiting the pinholes and the cabling to avoid scattering into the ground shields. Solid jacketed cables (such as aluminum jacketed RG405) which are pre-routed on the beamstop to a common patch panel should be considered as the best way to reduce noise and remove the need for a complicated baseline correction.

Even though we completely focused our analysis in this report on the B3 film, we suggest still using both the B3 and V2 films and attempting to correlate their dose-distances profiles so that additional sensitivity could be obtained near the end-point energy. A side shield may be needed on the wedges

to prevent edge-effect saturation of the more sensitive V2 film due to electron/low energy photon scatter into the sides of the wedges.

A final suggested change would be to produce more dose calibrations swatches between 0 and 1000 Gy. This would allow the neural network dose predictor to produce a smoother transition near the cut-off and should improve the precision of both the end-point energy prediction, as well as improve the fidelity of the shape of the peak and cut-off in the electron energy spectrum.

REFERENCES

[1] D. D. Bloomquist, R. W. Stinnett, D. H. McDaniel, J. R. Lee, A. W. Sharpe, and J. A. Halbleib. Saturn, A Large Area X-ray Simulation Accelerator. SAND87-0129C.

[2] J. R. Lee, M. A. Hedemann, J. A. Halbleib, A. W. Sharpe, V. J. Harper-Slaboszewicz, G. A. Carlson, R. J. Leeper, G. T. Baldwin, D. L. Fehl, W. A. Stygar, D. D. Bloomquist, J. D. Boyes, and L. M. Choate. The Saturn Flash X-ray Source. SAND88-2252A.

[3] M. A. Hedemann, J. R. Lee, J. A. Halbleib, G. A. Carlson, G. T. Baldwin, W. A. Stygar, R. J. Leeper, D. L. Fehl, A. W. Sharpe, L. M. Choate. Characterization of the Saturn Bremsstralung Source. SAND88-0198A.

[4] J. D. Boyes, J. S. Cap, G. M. Douglas, T. L. Franklin, J. M. Hart, H. C. Ives, S. J. Robischon, B. L. Smith, W. O. Stoppkotte, D. M. VanDeValde, E. A. Weinbrecht, and T. L. Woolston. Engineering Design of the Saturn Accelerator. SAND87-0303C.

[5] Ed Weinbrecht. Final Design Review Document for the Magnetically Insulated Transmission Line Module of Saturn. Work Package X72-01. May 21, 1986.

[6] (No authors listed). Saturn Baseline Document. February 14, 1986.

[7] "Standard Practice for dosimetry in an electron beam facility for radiation processing at energies between 300 keV and 25 MeV," ASTM E 1649-00, July 2000.

[8] G.X. Ding and D.W.O. Rogers. Energy spectra, angular spread and dose distributions of electron beams from various accelerators used in radiotherapy. April, 1995. http://www.irs.inms nrc ca/inms/irs/papers/PIRS439/pirs439.html.

[9] Timothy J. Webb. Theoretical Design and Experimentation of an Autoacceleration System For the Idaho State Induction Accelerator System (ISIS). Ph. D. Dissertation. Idaho State University. June 2007.

[10] I.D. Smith et al, "Design of a radiographic integrated test stand (RITS) based on a voltage adder, to drive a diode immersed in a high magnetic field", IEEE Trans. Plasma Sci., vol 28, pp 1653-1659, 2000.

[11] Timothy J. Webb, Kelly D. Hahn, Mark D. Johnston, Bryan V. Oliver, Dale R. Welch. Energy and Current Density Measurements of RITS-6 Large-Area Diode Electron Beam. IEEE TRANSACTIONS ON PLASMA SCIENCE, VOL. 38, NO. 4, APRIL 2010.

[12] GAFCHROMIC HD-V2 Film Specification and User Guide. Ashland Advanced Materials. Available at: http://www.gafchromic.com/documents/gafchromic-hdv2.pdf . Accessed 2020-06-30.

[13] B3 Radiochromic Film Dosimetry. Technical Memorandum. GEX Corporation. Release Date 2010-08-01. Available at: https://www.gexcorp.com/pdf/100-205_B3_Radiochromic_Film_Dosimetry_090110.pdf . Accessed 2020-06-30.

[14] T. Goorley, et al., "Initial MCNP6 Release Overview", Nuclear Technology, 180, pp 298-315 (Dec 2012).

[15] R. Jeraj, Paul J. Keall, and Patricia M. Ostwald. Comparisons between MCNP, EGS4 and experiment for clinical electron beams. Phys. Med. Biol. 44 (1999) 705–717.

[16] T.C. Wagoner *et al.* Differential-outputB-dot andD-dot monitors for current and voltage measurements on a 20-MA, 3-MV pulsed-power accelerator. Phys. Rev. ST Accel. Beams 11, 100401 (2008).

APPENDIX A. INTERPRETING B-DOT DATA

Typically, the method for processing B-dot signals involves a simple baseline offset subtraction following by an integration. For these B-dot signals we found that was insufficient. This appendix describes the additional steps needed to process the B-dot signals.

A.1. Method for cleaning B-dot data

The B-dot signals showed an unusual behavior after the main pulse with a long tail that looked like a capacitive charging effect. A Mathematica code was developed to compute an adjustable B-spline fit to the unintegrated signal to try to remove this effect. Figure 6-1 shows the semi-automated widget with an example signal. The widget automatically attempts to compute a B-spline fit to the data with the initial control points indicated by the cyan circles. The tail of the signal usually matched fairly well but the algorithm gets confused by the high frequency differential part of the signal around the main pulse. The widget allows manual tuning of the control points shown as the small bullseye markers. The user readjusts the control points by dragging them to match to the median signal. By making adjustments and clicking the *Recalculate BSpline* button, the widget will then subtract this baseline, integrate the signal and show the result. The goal is to produce an integrated signal that comes back to the starting baseline after the pulse. This is an iterative process and it was found that some of the signals cannot be made to come back to baseline using this technique.

The most difficult decision involves where to manually set the control point marker to indicate the baseline during the differential part of the signal. Setting this marker in the wrong place can result in the baseline returning to a non-zero constant value, however that is somewhat ignorable. We are most concerned with the pulse width of the signals and their peak values. Figure 6-2 shows an example of how to adjust the baseline to get the signal to return to zero at the end of the pulse.

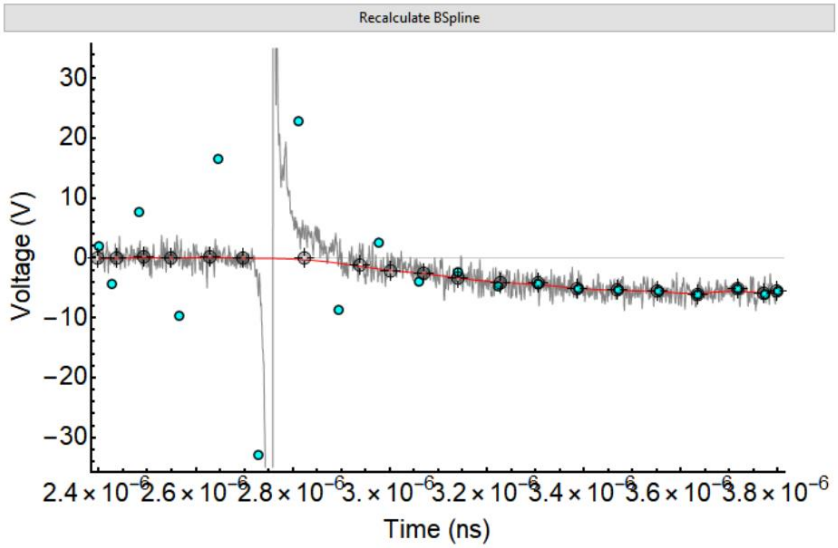

Figure 6-1. Mathematica widget used to manually remove the baseline of B-dot signal.

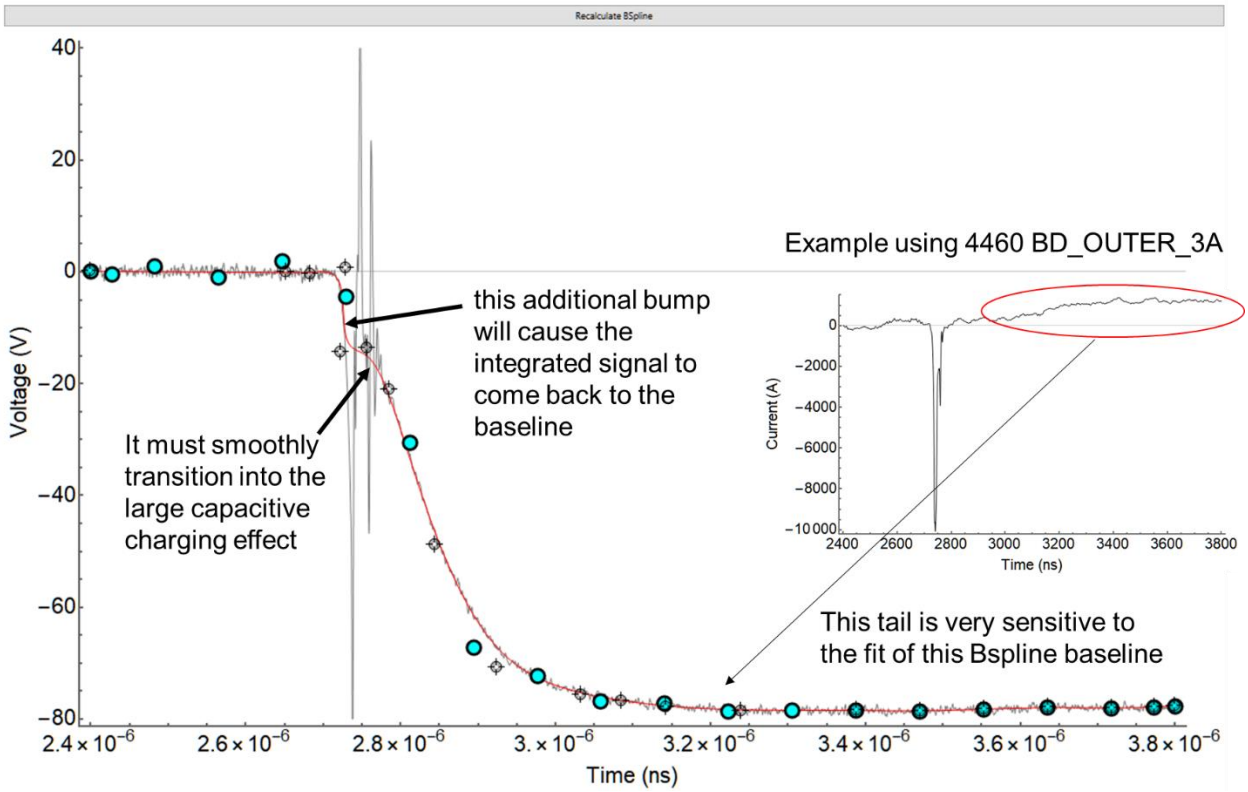

Figure 6-2. Diagram explaining some of the effects seen when trying to baseline the signals.

APPENDIX B. TRAINING THE NEURAL NETWORK

This appendix is a detailed description of how the neural network predictor was setup and trained to predict the dose value based on the pixel color of the scanned radiochromic films. Both the V2 and B3 films were trained using this method but it became clear that the V2 film was too sensitive to be able to extract a good maximum penetration depth and therefore determine an electron end-point energy. Therefore, only the B3 film is shown.

Mathematica 12.2 was used for both the imaging processing and the machine learning. Recent versions have implemented easy to use machine learning algorithms and the software also handles image processing tasks with ease.

B.1. Creating the training set

Each radiochromic film was scanned alongside the calibration swatches. For each film, the swatches were extracted from the scanned image and assigned their calibration dose values. The scanner had a 16-bit color resolution and produced RGB three color channel data: red, green, and blue. Each colored pixel is a point in RGB-space, essentially a three-dimensional data point. A huge association of doses and RGB values was created that ultimately gave us more than 150,000 training points, however with only 15 dose values.

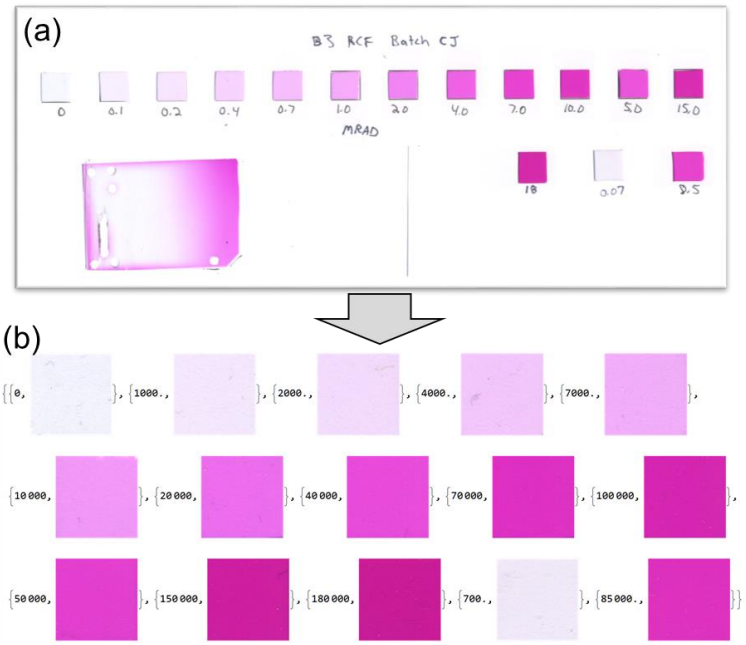

Figure 6-3. (a) The radiochromic film is scanned alongside the calibration swatches. (b) Image processing is used to extract the swatches into Mathematica.

The B3 film has a manufacturer specified useful dose range of 300 Gy to 160 kGy. Because the film turns from clear to an increasingly darker shade of magenta, that means that some color channels will be more useful than others in determining the correlation of color to dose. This is seen in Figure 6-4 when the calibration points are plotted in 3-D with the axes being the red, green, and blue color channels. We see that the green color channel is most able to resolve the high dose region whereas the red and blue channels are essentially saturated. For the low dose region, the blue channel is the most effective, however all channels are changing enough to be useful.

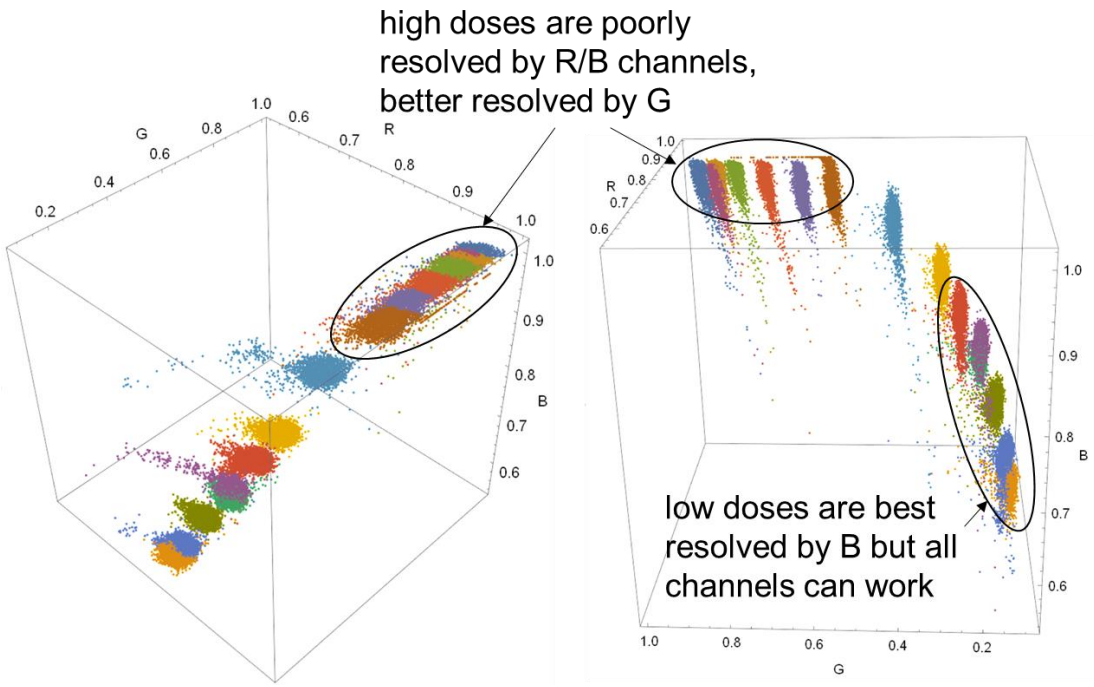

Figure 6-4. The calibration data can be considered a 3-D point cloud of RGB (Red/Green/Blue) values. The colored clouds of points represent the spread in values for a given dose calibration swatch.

B.2. Training the neural network

Training a machine learning algorithm in Mathematica uses the Predict function. This function is a general purpose machine learning predictor that can use a variety of training data and many different machine learning methodologies. It was found through trial and error that the Neural Network methodology was superior for this application.

Improperly setup neural networks can get "stuck" on the dose values in the training set (e.g. Figure 6-5). Initially we couldn't figure out how to overcome this problem. We sought the advice of Warren Davis, a machine learning SME from org. 1461. He suggested several things that could help. The order of the training set was randomized and 10% of the dataset was held back as a validation set. We also linearized the data by taking the log of the dose values. The zero dose values were first set to 1 Gy. Neural network algorithms can struggle with data over so many orders of magnitude. These fixes combined resulted in successfully training the algorithm to predict a smooth dose fall-off on our films.

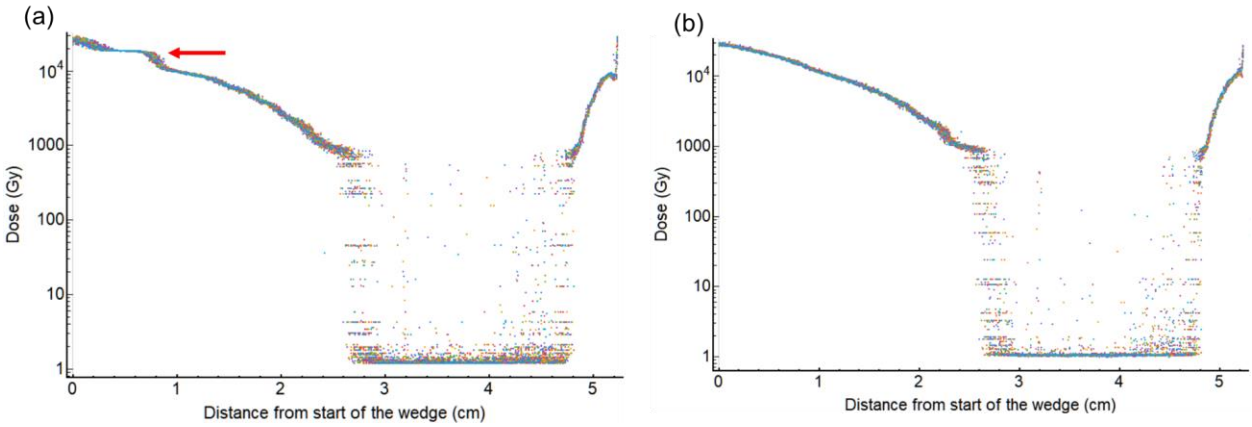

Figure 6-5. Improperly setup neural network predictors can get stuck on training set values. (a) shows the network getting stuck on the 20000 Gy training data (red arrow) while (b) has been setup correctly with linearized data and a validation set, avoiding this problem.

APPENDIX C. MCNP6 INPUT DECK FOR MONOENERGETIC DOSE-DISTANCE RESPONSE FUNCTIONS

This is an example for an energy of 0.4 MeV. A separate run would be performed for each desired energy.

[wedges_test040.i]

```
Webb's Wedges depth-dose, 0.4 MeV, extended block
C Cell cards
1 1 -2.7    -3 1 2 IMP:E,P=1  $aluminum block
2 3 -1.39  -1       IMP:E,P=1  $B3 film, middle
3 3 -1.39  -2       IMP:E,P=1  $V2 film, middle
4 3 -1.39  -4       IMP:E,P=1  $V2 film, top
5 3 -1.39  -5       IMP:E,P=1  $B3 film, top
6 2 -1.42  -6       IMP:E,P=1  $Kapton
7 1 -2.7    -7      IMP:E,P=1  $Al foil
9 0           3 4 5 6 7   IMP:E,P=0 $void
11 0          -11    IMP:E,P=0  $CC cell

C Surface cards
C  1 1 RCC 0 0 -1  0 0 2  5
1  1 RPP  0 4    -1.5 1.5    -0.0066 0  $ middle B3
2  1 RPP  0 4    -1.5 1.5    -0.0175 -0.0066 $middle V2
3  RPP  -0.5 4     -1.5 1.5     -0.7  0  $aluminum block
4  RPP  -0.5 4     -1.5 1.5      0 0.0109  $top V2
5  RPP  -0.5 4     -1.5 1.5      0.0109  0.0175  $top B3
6  RPP  -0.5 4     -1.5 1.5      0.0175  0.02258 $top kapton
7  RPP  -0.5 4     -1.5 1.5      0.02258 0.024358 $top al foil
10 PZ  0.024358
11 RPP  -0.5 4    -1.5 1.5       0.024  0.025   $for CC cell

C Data cards
mode E P
cut:E j 0.01
cut:P j 0.02
DBCN   17j 1
m1 13000 1
C                                   Kapton polyimide film  p = 1.420
m2    1001      -2.6362     6000     -69.1133     7000      -7.3270
        8000     -20.9235
m3 6000 10   1000 8  8000  4      $ film approximation
*TR1 0 0 0  7.4 90 97.4   90 0 90   82.6 90 7.4
*TR2 0 0 0  7.4 90 97.4   90 0 90   82.6 90 7.4
SDEF Par=3 erg=0.4 sur=10 dir=-1  CCC=11 Z=0.024358 X=D1 Y=D2 Vec=0 0 1
SI1 -0.5 4
SP1 0 1
SI2 -1.5 1.5
```

```
SP2 0 1
TMESH
 RMESH13  trans 2
 CORA13 0 399I 4
 CORB13 -1 1
 CORC13  -0.0066 0
 RMESH23  trans 2
 CORA23 0 399I 4
 CORB23 -1 1
 CORC23  -0.0175 -0.0066
ENDMD
PRDMP j -30 1 3
print -86 -10 -170 110
NPS 1E8
```

This page left blank

DISTRIBUTION

Email—Internal

Name	Org.	Sandia Email Address
Bryan Oliver	01340	bvolive@sandia.gov
Debra Kirshner	01342	dskirsc@sandia.gov
Peggy Christensen	01343	pjchris@sandia.gov
Keith Cartwright	01351	klcartw@sandia.gov
Timothy Pointon	01351	tdpoint@sandia.gov
David Sirajuddin	01351	dsiraju@sandia.gov
Chris Grabowski	01385	tcgrabo@sandia.gov
Jonathan Douglass	01651	jddougl@sandia.gov
Brian Hutsel	01651	bthutse@sandia.gov
Mark Savage	01651	mesavag@sandia.gov
Michael Mazarakis	01656	mgmazar@sandia.gov
Timothy Renk	05499	tjrenk@sandia.gov
Ken Struve	05499	kwstruv@sandia.gov
Technical Library	01977	sanddocs@sandia.gov

This page left blank

This page left blank

Sandia National Laboratories

Sandia National Laboratories is a multimission laboratory managed and operated by National Technology & Engineering Solutions of Sandia LLC, a wholly owned subsidiary of Honeywell International Inc. for the U.S. Department of Energy's National Nuclear Security Administration under contract DE-NA0003525.